catalysts

MDPI

Article

Catalytic Oxidative Decomposition of Dimethyl Methyl Phosphonate over CuO/CeO_2 Catalysts Prepared Using a Secondary Alkaline Hydrothermal Method

Weimin Kong [1,2,†], Shuyuan Zhou [2,*,†], Xuwei Wang [1,2], Qingrong He [2], Piaoping Yang [1,*], Ye Yuan [3,*] and Yanchun Dong [2,*]

1 Key Laboratory of Superlight Materials and Surface Technology, Ministry of Education, College of Material Sciences and Chemical Engineering, Harbin Engineering University, Harbin 150001, China
2 State Key Laboratory of NBC Protection for Civilian, Beijing 102205, China
3 Key Laboratory of Polyoxometalate Science of Ministry of Education, Northeast Normal University, Changchun 130024, China
* Correspondence: zhoushuyuan@sklnbcpc.cn (S.Z.); yangpiaoping@hrbeu.edu.cn (P.Y.); yuany101@nenu.edu.cn (Y.Y.); dongyanchun@sklnbcpc.cn (Y.D.)
† These authors contributed equally to this work.

Abstract: Bimetallic synergism plays an important role in lattice-doped catalysts. Therefore, lattice-doped bimetallic CuO/CeO_2 catalysts were prepared by secondary alkaline hydrothermal reaction. During this process, the CeO_2 nanomaterials were partially dissolved and recrystallized; thus, Cu ions were doped into the CeO_2 lattice. The physical and chemical properties of CeO_2, CuO/CeO_2, and CuO were investigated. H_2 temperature-programmed reduction characterization showed that the oxidation activity of CuO/CeO_2 was significantly improved. X-ray photoelectron spectroscopy results showed that electron transfer occurred between Ce and Cu in the CuO/CeO_2 catalyst. Additionally, Raman characterization confirmed the strong interaction between Cu and Ce. After CuO was loaded, the thermal catalytic decomposition performance of the catalyst was significantly improved with respect to the sarin simulant dimethyl methyl phosphonate (DMMP); with an increase in the Cu/Ce ratio, the performance first strengthened and then weakened. Additionally, the reaction tail gas and catalyst surface products were analyzed using mass spectrometry and ion chromatography, and the changes in the surface products during the thermal catalytic decomposition of DMMP were characterized at different temperatures using in situ diffuse reflectance infrared Fourier transform spectroscopy. Finally, the catalytic reaction pathways of DMMP on CeO_2, CuO/CeO_2, and CuO were inferred. The study results not only demonstrate an effective catalyst for the removal of nerve agent but also a feasible preparation method for lattice-doped bimetallic catalysts in the field of environmental protection.

Keywords: nerve agent; dimethyl methyl phosphonate; thermocatalytic; CuO/CeO_2

check for updates

Citation: Kong, W.; Zhou, S.; Wang, X.; He, Q.; Yang, P.; Yuan, Y.; Dong, Y. Catalytic Oxidative Decomposition of Dimethyl Methyl Phosphonate over CuO/CeO_2 Catalysts Prepared Using a Secondary Alkaline Hydrothermal Method. *Catalysts* **2022**, *12*, 1277. https://doi.org/10.3390/catal12101277

Academic Editors: Yaqiong Su, Jin-Xun Liu and Sen Lin

Received: 30 August 2022
Accepted: 16 October 2022
Published: 19 October 2022

1. Introduction

The threat posed by chemical warfare agents (CWAs) in terrorist incidents, wars, and conflicts has not yet been addressed. Research on the degradation of CWAs is crucial for human health and national security [1]. Traditional and currently used protection methods involve adsorption through carbon-based materials. However, the adsorption capacity of carbon-based materials is limited, and weak adsorption can lead to secondary pollution [2,3]. Recent studies have shown that the catalytic oxidation and decomposition of CWAs by metal oxides is an effective method, with the advantage of destroying the molecular structure of CWAs and generating low-toxicity or non-toxic products [4–8]. From the perspective of CWAs treatment, protection time, which specifically refers to the time required for complete conversion of CWAs, is an important parameter for evaluating catalyst performance [9].

Sarin, a typical nerve CWA, has been repeatedly used in military conflicts and terrorist attacks, causing massive casualties of troops and innocent civilians [2]. Therefore, it is significant to study the catalytic degradation of sarin. Sarin is an organic phosphate ester. The chemical structure of sarin is shown in Figure 1a. Its poisoning mechanism involves the combination of organophosphate ester with the acetylcholinesterase (AchE) to form a stable phosphoryl cholinesterase, which inhibits the activity of the enzyme and paralyzes the nervous system [1,10]. The poisoning mechanism of sarin is similar to that of organophosphorus pesticides. Dimethyl methyl phosphonate (DMMP) is often used as a simulant for organophosphorus pesticides [11]. Owing to its similar molecular structure (Figure 1b), low toxicity, and similar poisoning mechanism, DMMP is also frequently used as a simulant for sarin [12–14].

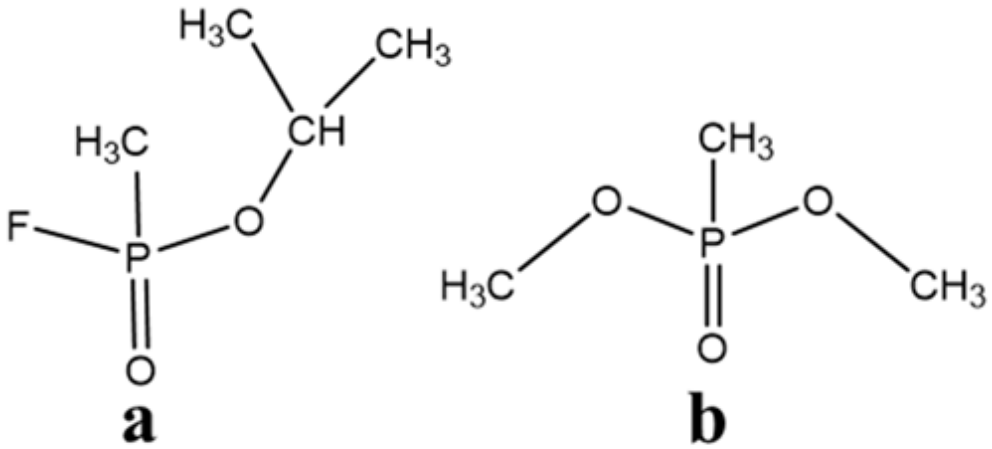

Figure 1. The chemical structure of (**a**) sarin and (**b**) DMMP.

Metal oxides, such as Al_2O_3 [15], MgO [16], Y_2O_3 [7], TiO_2 [17], Fe_2O_3 [18], CuO [19,20], CeO_2 [21,22], and others, have a good P-OCH_3 bond-breaking ability and are widely used for DMMP decomposition. The decomposition products of DMMP on monovalent metal oxides include methanol, dimethyl ether, and methylphosphonic acid, whereas the products on variable metal oxides can be further oxidized to CO, CO_2, and PO_X. The main reason for this is that the redox couple of the metal ions in the reaction can provide a low-energy reaction path for the oxidation reaction.

Variable-valence CeO_2 has an excellent oxygen storage/release capacity and can be reversibly changed between Ce^{3+} and Ce^{4+}, accompanied by the generation and elimination of oxygen vacancies, making it widely applicable in heterogeneous catalysis [23]. Chen et al. reported that DMMP completely decomposed on ceria films using vacuum heating, forming products of methanol, formaldehyde, CO, and H_2 [21]. Li et al. studied the interaction of DMMP with CeO_2 on different surfaces using density functional theory [22]. Loading transition metal oxides onto CeO_2 nanomaterials is an effective method to further improve the catalytic activity of the catalysts. CuO/CeO_2 is one of the most widely studied two-component, non-noble metal catalysts, and the strong interaction between CuO and CeO_2 promotes electron transfer between Cu and Ce, as well as oxygen migration in CeO_2. Presently, CuO/CeO_2 catalysts are commonly used in CO oxidation and hydrogenation reactions, VOC degradation, water gas shift reactions, and CO_2 hydrogenation reactions [24–28]. However, CuO/CeO_2 catalysts have not yet been studied for the catalytic oxidation of DMMP. Therefore, the performance and reaction mechanism of the CuO/CeO_2 catalyst for the thermal catalytic decomposition of DMMP were comprehensively investigated in this study.

Traditional preparation methods for CuO/CeO_2 include the one-time hydrothermal, impregnation, and deposition precipitation methods [29–32]. George et al. prepared a CuO/CeO_2 catalyst using ammonia solution and acid solution post-synthesis modification methods and reported significantly improved catalytic CO activity [33,34]. Zhou et al. prepared highly dispersed CuO/CeO_2 catalysts using a secondary solvothermal method

(ethanol as the solvent) to mix a CeO_2 support with $Cu(NO_3)_2$ dissolved in an ethanol solution, then dried and calcined it after the reaction [35]. Inspired by the above method, solid CeO_2 was mixed with a $Cu(NO_3)_2$ solution, and a given concentration of NaOH solution was added for the secondary alkaline hydrothermal method. The addition of NaOH resulted in the dissolution and recrystallization of CeO_2 during the reaction. During this process, Cu was doped into the CeO_2 lattice, which increased the interaction between Cu and Ce, promoted electron transfer between Cu and Ce, and formed a Cu-V-Ce (V is donated as oxygen vacancy) structure. Thus, the performance of the CuO/CeO_2 catalyst further improved.

The traditional impregnation and deposition precipitation methods have low utilization rates of raw materials, and when the loading amount increased, serious agglomeration occurs. In our study, high-loading and uniform-distribution CuO were prepared using the secondary alkaline hydrothermal method. This method is characterized by a high utilization rate of raw materials. According to the ICP results obtained in the present study, the theoretical loading of CuO is comparable to actual loading.

In this study, three types of CeO_2, CuO/CeO_2, and CuO catalysts were prepared. First, a CeO_2 support was prepared using a hydrothermal method. Secondly, CuO/CeO_2 catalysts with varying Cu/Ce ratios were prepared using the CeO_2 support mixed with $Cu(NO_3)_2$ solution and NaOH solution by the alkaline hydrothermal method. In order to study the changes in physicochemical properties and catalytic performance after CeO_2-supported CuO, CuO was also prepared by a hydrothermal method for comparison. The structure was characterized using X-ray diffraction (XRD) and transmission electron microscopy (TEM). The surface elemental distribution, redox properties, and surface intermediate products were analyzed using X-ray photoelectron spectroscopy (XPS), H_2-temperature-programmed reduction (H_2-TPR), O_2-temperature-programmed desorption (O_2-TPD), and in situ diffuse reflectance infrared Fourier transform spectroscopy (in situ DRIFTS). The reaction path was deduced for the thermal decomposition of DMMP on the catalyst. In this study, CuO/CeO_2 catalysts with high loading and uniform distribution were synthesized, and the initial morphology of CuO was not changed. The dissolution and recrystallization of CeO_2 in the alkali–thermal process promoted the doping of Cu into the CeO_2 lattice, and bimetallic synergism enhanced the catalytic performance. The results of this study provide a reference for the design and optimization of CWA decomposition catalysts.

2. Results and Discussion

2.1. Characteristics of CuO/CeO_2 Catalysts

The as-prepared materials were characterized using XRD to identify crystal phases (Figure 2). The Figure 2 shows that the CeO_2 and CuO diffraction patterns match the characteristic peaks of the fluorite structure of CeO_2 (JCPDS 34-0394) and the monoclinic structure of CuO (JCPDS 80-1916), respectively. The intensity of the CuO diffraction peaks gradually increased with increased Cu/Ce ratio, and some CeO_2 diffraction peaks disappeared. When the Cu/Ce ratio was 10%, weak diffraction peaks appeared at 36.49° and 38.68°, corresponding to the (−111) and (111) crystal planes of the CuO diffraction peaks, respectively. This phenomenon may have been caused by the low loading of CuO. When the Cu/Ce ratio was 50%, the intensities of the diffraction peaks of the (−111) and (111) crystal planes increased, and new diffraction peaks appeared at 48.6° and 61.6°, corresponding to the (−202) and (−113) crystal planes of CuO, respectively. The crystalline size of the catalyst was calculated using the Scherrer equation, as shown in Table 1. Owing to the smaller Cu diffraction peaks in 10%Cu/Ce and 20%Cu/Ce, the crystalline size of CuO could not be calculated. Table 1 shows that the grain sizes of CeO_2 and CuO prepared using the secondary alkaline method did not change significantly.

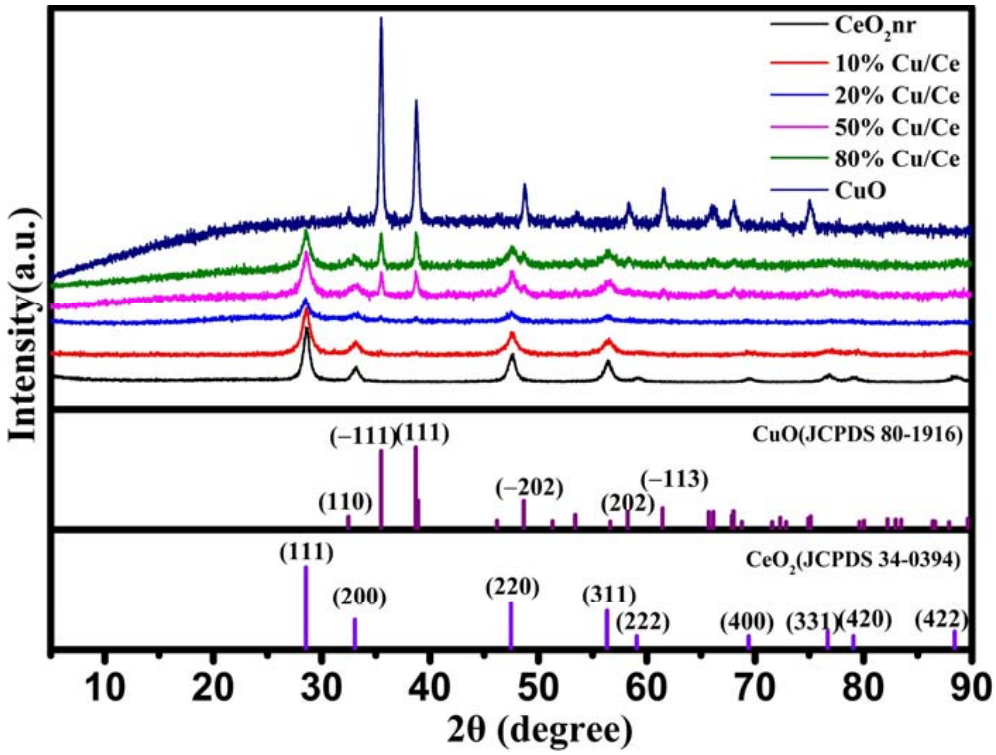

Figure 2. XRD patterns of the as-prepared CuO/CeO_2 catalysts.

Table 1. Physical properties of the as-prepared CuO/CeO_2 catalysts.

Catalyst	CeO_2 Crystallinity Size (nm)	CuO Crystallinity Size (nm)	Cu/Ce (wt%)	BET (m^2/g)
CeO_2nr	10.8	/	/	91
10%Cu/Ce	9.01	/	10.51%	91.5
20%Cu/Ce	10.01	/	23.92%	77.5
50%Cu/Ce	10.59	28.14	53.06%	66.6
80%Cu/Ce	10.93	28.14	88.32%	63.2
CuO	/	21.41	/	23.4

The actual ratio of Cu/Ce determined by ICP-OES was higher than the theoretically calculated value (Table 1), indicating that CeO_2 was partially dissolved in the secondary alkaline hydrothermal environment. The specific surface area (S_{BET}) of the samples was determined using the N_2 adsorption–desorption method. As shown in Table 1, the S_{BET} of the CuO/CeO_2 catalyst decreased, mainly due to the formation of sheet-morphology CuO (Figure 3f). The S_{BET} of sheet-morphology CuO is significantly lower than that of CeO_2 (Table 1). Therefore, the S_{BET} of the CuO/CeO_2 catalyst decreased with increased in CuO doping. Moreover, the S_{BET} of 50% Cu/Ce and 80% Cu/Ce catalysts decrease more significantly compared with that of 10% Cu/Ce and 20%Cu/Ce catalysts as a result of the appearance of a large amount of sheet-morphology CuO (Figure 3d,e) on CeO_2 nanorods.

Figure 3 shows a TEM image of the CuO/CeO_2 catalyst. Figure 3a,f shows that the morphologies of pure CeO_2 and CuO were nanorods and nanoplates, respectively. Figure 3b–e shows TEM images of the CuO/CeO_2 catalysts with Cu/Ce ratios of 10, 20, 50, and 80%, respectively. The morphology of the CeO_2 nanorods did not change after loading with CuO, and when the Cu/Ce ratio was 50 and 80%, CuO nanoplates began to appear (Figure 3d,e). Figure 4 shows EDX images of the Cu/Ce catalysts with varying loading ratios, demonstrating that Cu was evenly distributed on the CeO nanorods (Figure 4a,b).

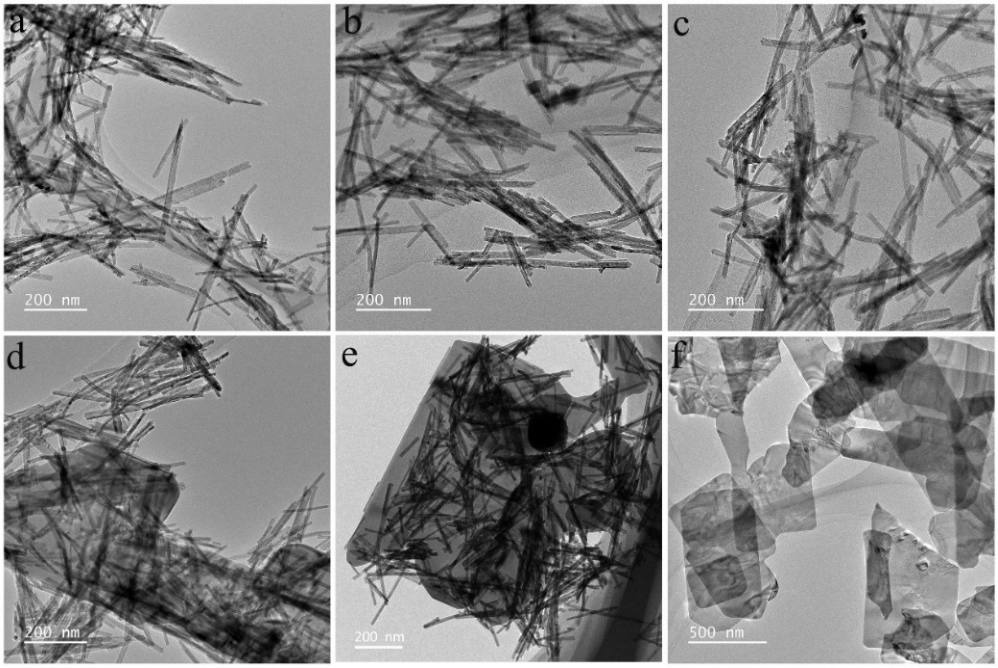

Figure 3. TEM images of the CuO/CeO_2 catalysts: (**a**) CeO_2nr, (**b**) 10%Cu/Ce, (**c**) 20%Cu/Ce, (**d**) 50%Cu/Ce, (**e**) 80%Cu/Ce, and (**f**) CuO.

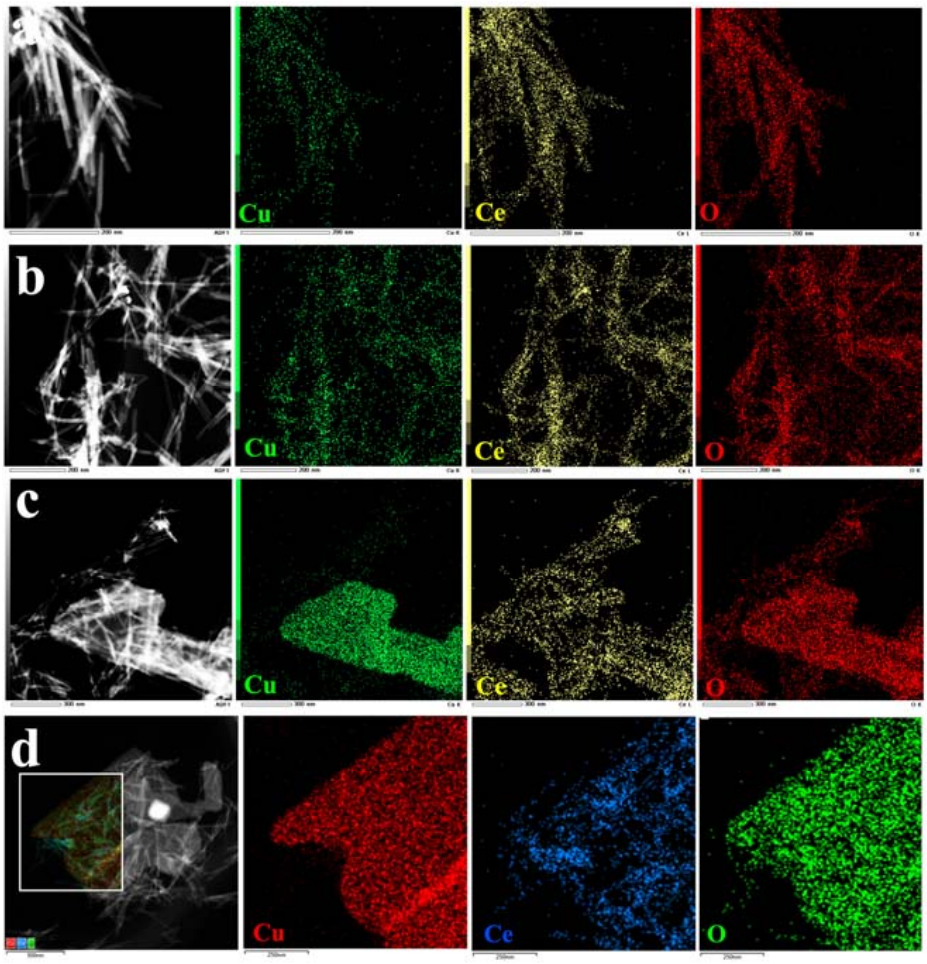

Figure 4. EDX maps of various elements in the CuO/CeO_2 catalysts: (**a**) 10%Cu/Ce, (**b**) 20%Cu/Ce, (**c**) 50%Cu/Ce, and (**d**) 80%Cu/Ce.

Figure 5 shows HRTEM images of the catalysts. The exposed (111) and (200) crystal planes of the CeO_2 nanorods correspond to the lattice fringes at 0.31 and 0.28 nm, respectively (Figure 5a); the exposed (020) crystal planes of the CuO nanoplates correspond to the lattice fringes at 0.17 nm (Figure 5f). Figure 4c–e shows that a lattice spacing of 0.29 nm appeared with increasing CuO load due to the change in lattice spacing caused by the doping of Cu atoms into the CeO_2 lattice.

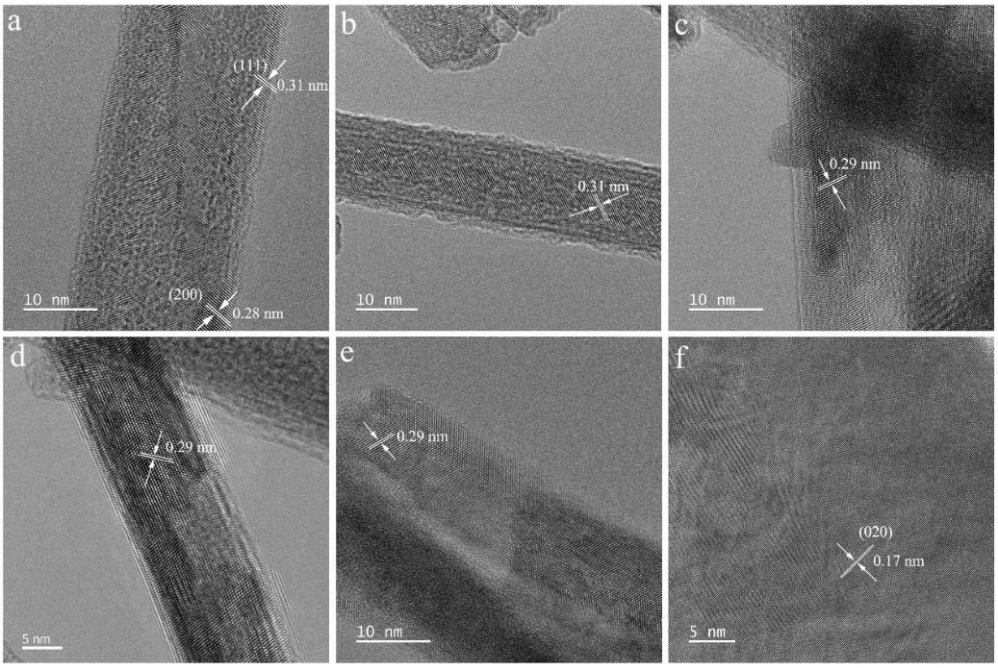

Figure 5. HRTEM images of the CuO/CeO_2 catalysts: (**a**) CeO_2nr, (**b**) 10%Cu/Ce, (**c**) 20%Cu/Ce, (**d**) 50%Cu/Ce, (**e**) 80%Cu/Ce, and (**f**) CuO.

The oxidation activity of the catalyst material was characterized using H_2-TPR (Figure 6a and Table 2). There are usually two reduction peaks of CeO_2: a peak at approximately 675 °C corresponding to the surface oxygen reduction peak of CeO_2 and a peak at approximately 835 °C corresponding to the bulk oxygen reduction peak of CeO_2 [36]. A broad peak appeared in CuO at 170–500 °C, which may be due to the closeness of the surface oxygen and bulk oxygen reduction peaks of CuO, such that the two peaks cannot be completely separated. CuO/CeO_2 has three main peaks at 170–202 °C, 250 °C, and 275 °C, which are denoted by α, β, and γ, respectively. The α peak corresponds to CuO_x, which interacts strongly with CeO_2; the β peak corresponds to CuO_x, which interacts weakly with CeO_2; and the γ peak is attributed to bulk CuO [37]. The H_2-TPR diagram (Figure 6) clearly shows that after CuO was loaded onto CeO_2, the reduction temperature of the CuO/CeO_2 catalyst was significantly lower than that of the CeO_2, indicating that the loaded catalyst had more active oxygen. H_2 consumption amounts of as-prepared catalyst were calculated using H_2-TPR (Table 2). As shown in Table 2, the theoretical and the calculated value of H_2 consumption increased with an increase in the Cu/Ce loading ratio. The calculated hydrogen consumption amount of 10%Cu/Ce catalyst exceeded theoretical values; however, with an increase in the Cu/Ce ratio, the theoretical calculated value exceeded the calculated value, implying a interaction between CeO_2 and CuO species [38]. Evidently, the addition of CuO improved the CeO_2 oxidation activity.

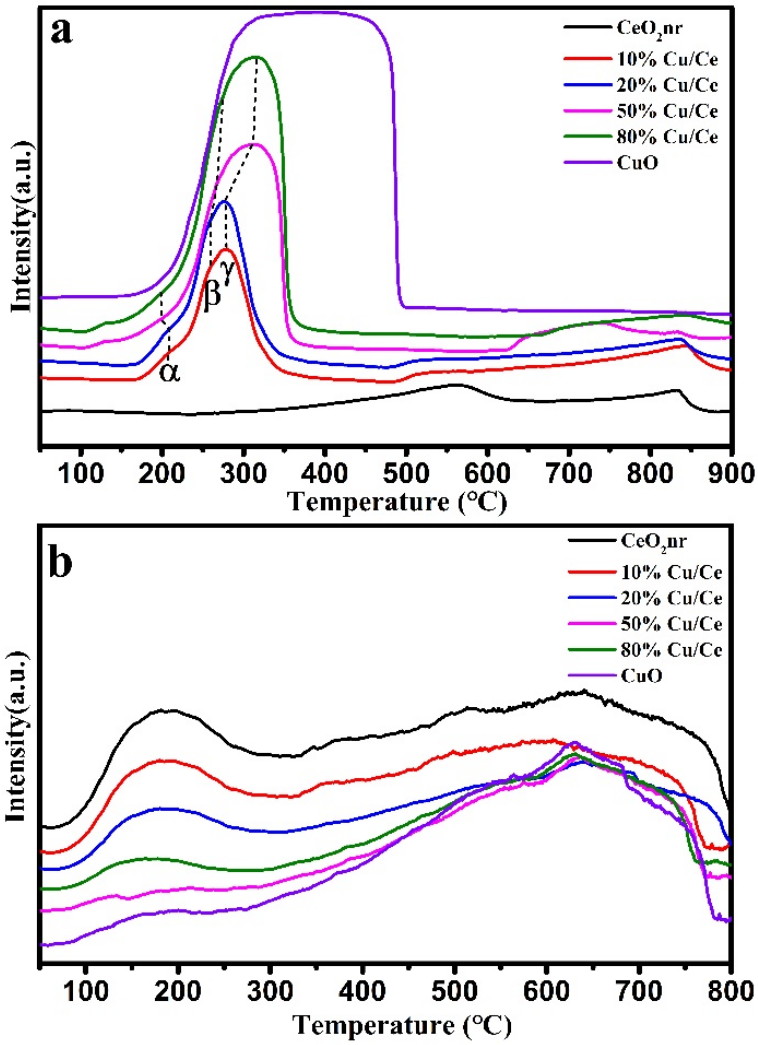

Figure 6. (**a**) H_2-TPR and (**b**) O_2-TPD profiles of the CuO/CeO_2 catalysts.

Table 2. H_2 consumption amounts of as-prepared catalyst calculated by H_2-TPR.

Catalyst	T_R (°C)			Total H_2 Consumption (mmol/g_{cat})	Theoretical H_2 Consumption (mmol/g_{cat})
	α	β	γ		
10%Cu/Ce	207	260	278	2.6	1.53
20%Cu/Ce	207	259	276	2.89	3.09
50%Cu/Ce	199	268	315	3.22	5.53
80%Cu/Ce	197	271	316	3.62	7.46
CuO		375		6.75	15.75
CeO_2nr		549		1.53	/

O_2-TPD tests were performed on the CuO/CeO_2 catalysts, CeO_2, and CuO to investigate the desorption behavior of oxygen (Figure 6b and Table 3). Two types of oxygen exist in the catalyst, namely surface-adsorbed oxygen and lattice oxygen [39]. The peak at 180 °C is related to chemisorbed oxygen around the oxygen vacancies, and the peak at 640 °C is related to oxygen escaping from the lattice. As shown in Table 3, with an increase in the Cu/Ce ratio, the amount of oxygen adsorbed at low temperatures decreased, and the lattice oxygen at high temperatures increased.

Table 3. The amounts of O_2 desorbed by O_2-TPD from as-prepared catalyst samples.

Catalyst	Peak Position (°C)	Desorption O_2 (mmol/g_{cat})	Peak Position (°C)	Desorption O_2 (mmol/g_{cat})	Total Desorption O_2 (mmol/g_{cat})
CeO_2nr	180	1.26	643	1.61	2.87
10%Cu/Ce	180	0.99	641	1.67	2.66
20%Cu/Ce	182	0.72	640	1.79	2.51
50%Cu/Ce	180	0.51	652	1.9	2.41
80%Cu/Ce	/	/	658	2.15	2.15
CuO	/	/	660	2.34	2.34

XPS characterizations were used to obtain the composition information and determine the chemical state on the surface of CeO_2, CuO, and CuO/CeO_2. Figure 7 shows the Ce 3d XPS spectra of the CeO_2 and CuO/CeO_2 catalysts, which are deconvoluted into ten peaks [36,40,41]. The Ce 3d spectra are composed of two-group spin orbitals of the overlapping peaks, labeled as U_0–U```for $3d_{3/2}$ and V_0–V```for $3d_{5/2}$. The binding energy peaks of V (882.14 eV), V``(888.51 eV), V```(898.05 eV), U (900.63 eV), U``(907.32 eV), and U```(916.45 eV) are related to Ce^{4+}, whereas the binding energy peaks of V_0 (880.2 eV), V`(884.7 eV), $U_0$ (898.65 eV), and U`(903.09 eV) are associated with Ce^{3+}. The Ce^{3+} content was calculated using the peak area ratio of $Ce^{3+}/(Ce^{3+} + Ce^{4+})$, and the results are listed in Table 4. The Ce^{3+} content decreased after loading CuO. It has been speculated that a reversible reaction of $Ce^{3+} + Cu^{2+} \leftrightarrow Ce^{4+} + Cu^{+}$ and $2Ce^{3+} + Cu^{2+} \leftrightarrow 2Ce^{4+} + Cu^{0}$ occurs on the surface of the CuO/CeO_2 catalyst [42–44].

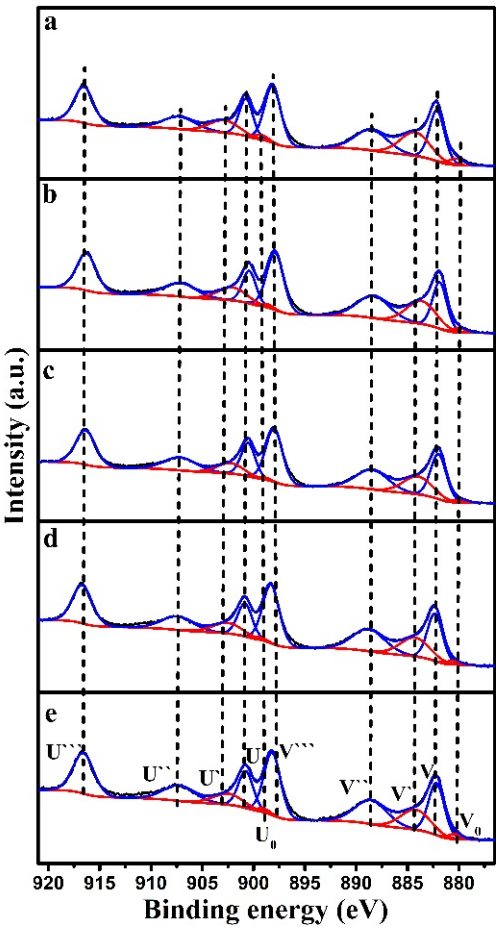

Figure 7. Ce 3d XPS spectra of the CuO/CeO_2 catalysts: (**a**) CeO_2nr, (**b**) 10%Cu/Ce, (**c**) 20%Cu/Ce, (**d**) 50%Cu/Ce, and (**e**) 80%Cu/Ce.

Table 4. XPS and Raman catalytic performance characterization.

Catalyst	XPS				Raman		Protection Time (min)
	Ce^{3+}	$O\beta/O_{all}$	$O\alpha/O_{all}$	$(Cu^0+Cu^+)/Cu^{2+}$	F_{2g} (cm^{-1})	I_D/I_{F2g}	
CeO_2nr	23.81%	26.98%	73.02%	/	463	0.04	140
10%Cu/Ce	22.77%	32.28%	67.72%	1.55	456	0.031	252
20%Cu/Ce	18.69%	31.23%	68.77%	2.21	445	0.052	266
50%Cu/Ce	18.86%	24.12%	75.88%	2.33	453	0.083	322
80%Cu/Ce	18.78%	22.13%	77.87%	2.44	453	0.064	140
CuO	/	33.64%	66.36%	/	/	/	56

Figure 8 shows the Cu 2p spectra and Cu LMM Auger spectra of the CuO/CeO_2 catalysts, where two characteristic peaks are visible, namely Cu $2p_{3/2}$ and Cu $2p_{1/2}$, along with a broad satellite peak in the Cu 2p spectra. The peaks centered at 934 and 954 eV correspond to Cu $2p_{3/2}$ and Cu $2p_{1/2}$, respectively, and the broad satellite peak is in the range of 937–947 eV. The peaks located at 934 eV and the corresponding satellite peaks are associated with Cu^{2+}, and the peaks located at 932–933 eV are associated with Cu^+ or/and Cu^0 [38,45]. The two reduced states (Cu^+ and Cu^0) are difficult to distinguish in the Cu 2p spectra [46–49]. In order to distinguish Cu^+ and Cu^0, Auger Cu LMM spectra were used. The broad feature in the kinetic energy spectra consists of three peaks at 917.5 eV, 913.2–916.0 eV, and 918.5 eV–919 eV, which are assigned to Cu^{2+}, Cu^+, and Cu^0 species, respectively [45,50–52]. Although the Cu LMM Auger spectra show that both Cu^0 and Cu^+ occur simultaneously in the prepared catalysts, the presence of Cu^0 species possible due to the photoreduction in the XPS test [37,49]. Table 4 presents the calculated Cu^0 and Cu^+ to Cu^{2+} ratios; it is clear that $(Cu^0 + Cu^+)/Cu^{2+}$ is related to the change in Ce^{3+} content (ΔCe^{3+}), which further indicates that reversible reactions of $Ce^{3+} + Cu^{2+} \leftrightarrow Ce^{4+} + Cu^+$ and $2Ce^{3+} + Cu^{2+} \leftrightarrow 2Ce^{4+} + Cu^0$ occurred on the surface of the CuO/CeO_2 catalyst. The $(Cu^0 + Cu^+)/Cu^{2+}$ of 20%Cu/Ce, 50%Cu/Ce, and 80%Cu/Ce were nearly the same and correspond to a minimal change in ΔCe^{3+}.

Figure 9 shows that the O1s spectra of the CeO_2, CuO, and CuO/CeO_2 catalysts were deconvoluted into two distinct peaks [36]. The low-binding-energy peak located at 528.5–529.5 eV (denoted as Oα) was attributed to surface lattice oxygen. The higher-binding-energy peak located at 530–531.5 eV (denoted as Oβ) was attributed to oxygen vacancies, surface-adsorbed O^{2-}/O^-, surface-adsorbed O_2, hydroxyl groups, and carbonates [39,53]. The Oα and Oβ contents were calculated based on the areas of the deconvoluted peaks (Table 4). With an increase in the Cu/Ce ratio, the Oβ content decreased, whereas the Oα content increased; this trend is consistent with the O_2-TPD results.

Visible Raman spectroscopy provides additional information about the lattice vibrations and internal defects of catalysts. Figure 10 shows that a strong band was detected at 450–460 cm^{-1}, which was ascribed to the Raman-active vibrational F_{2g} mode of CeO_2 with a fluorite-type structure. Another broad peak located at approximately 598 cm^{-1} was also detected (Figure 10 inset), which corresponds to the defect-induced (D) mode associated with O vacancies caused by the presence of Ce^{3+} [36]. The F_{2g} mode of CeO_2 shifted from 463 to 445 cm^{-1} for the CuO/CeO_2 catalysts, which is generally attributed to the shrinkage and distortion of the CeO_2 lattice caused by the electronic redistribution of the Cu-V-Ce structure. The ratio of the two peak intensities between the defect-induced (D) mode and the F_{2g} mode (I_D/I_{F2g}) represents the relative concentration of O vacancies (Table 4) [54,55]. The I_D/I_{F2g} first increased and then decreased with an increase in the Cu/Ce ratio, and 50%Cu/Ce exhibited the highest O vacancy concentration of 0.083.

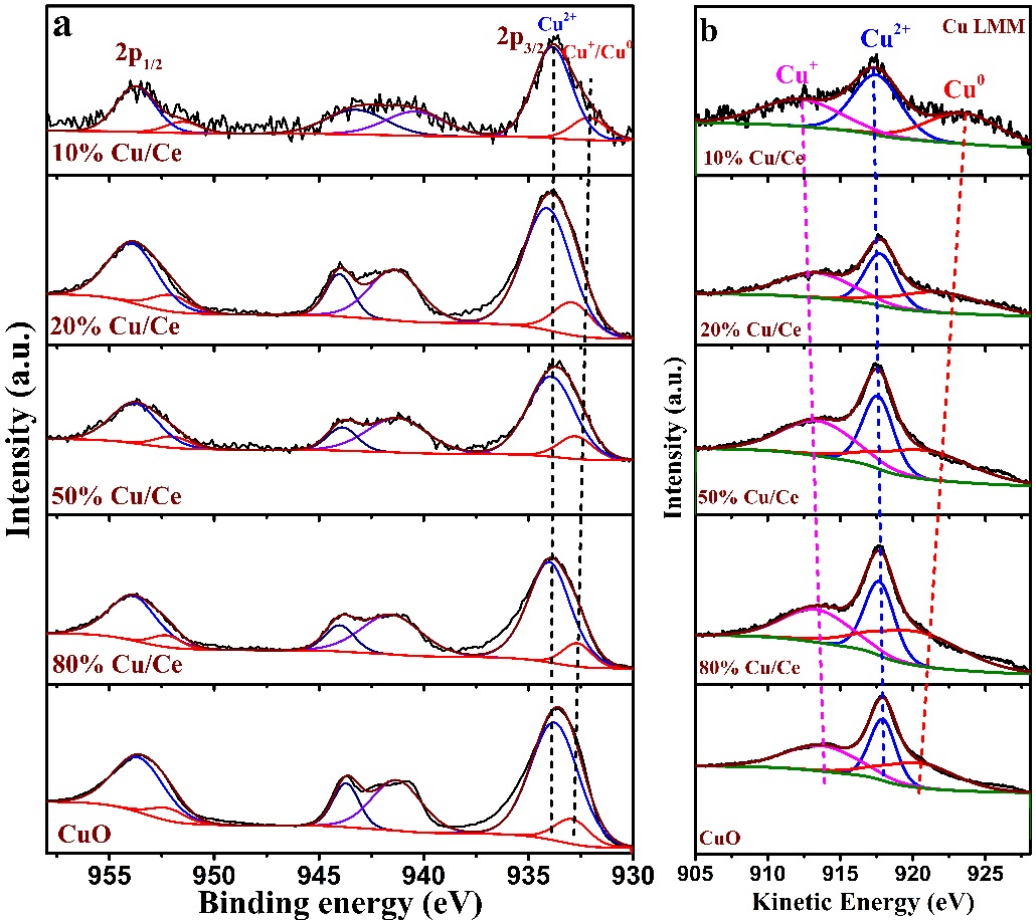

Figure 8. (**a**) Cu 2p XPS spectra and (**b**) Cu LMM spectra of the CuO/CeO_2 catalysts.

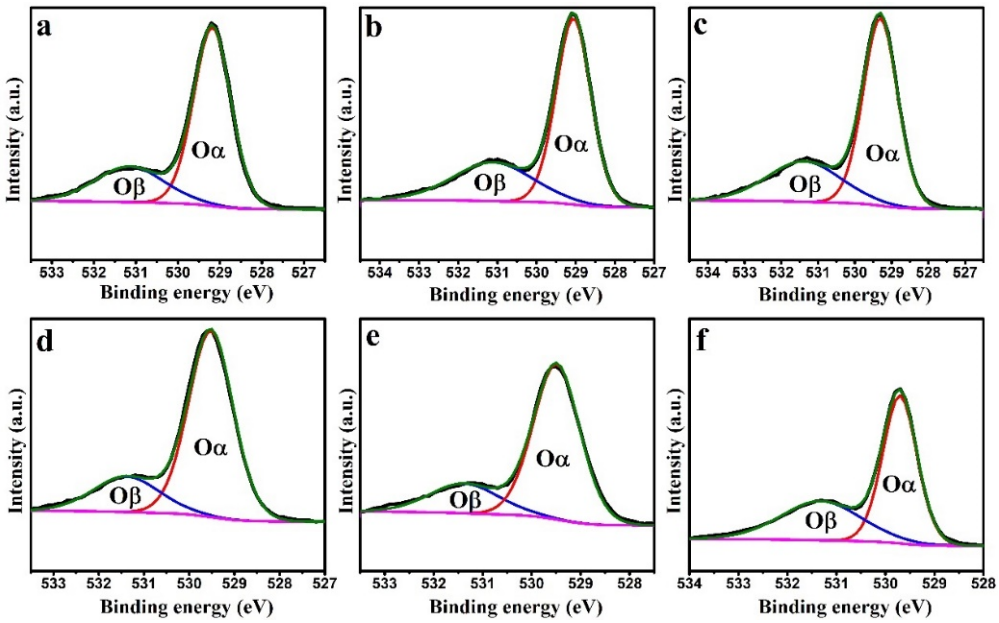

Figure 9. O1s XPS spectra of the CuO/CeO_2 catalysts: (**a**) CeO_2, (**b**) 10%Cu/Ce, (**c**) 20%Cu/Ce, (**d**) 50%Cu/Ce, (**e**) 80%Cu/Ce, and (**f**) CuO.

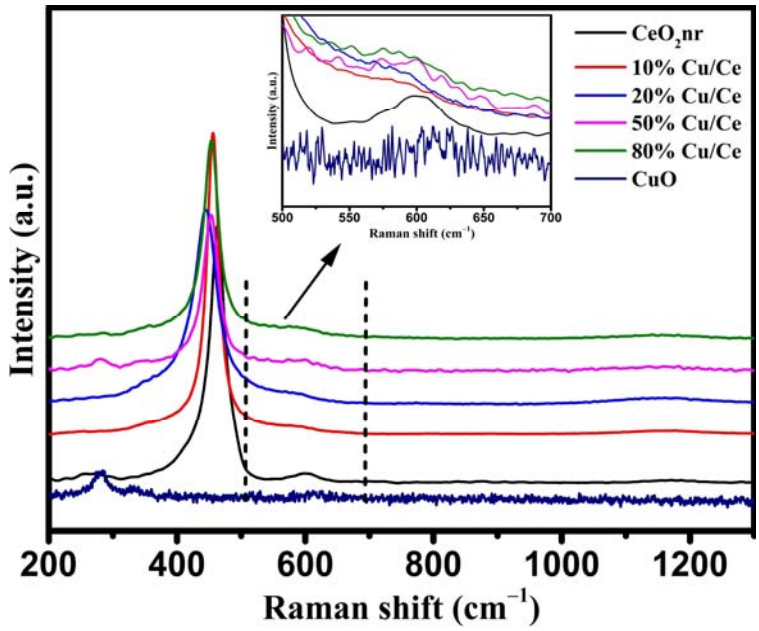

Figure 10. Raman spectra of the CeO_2-supported CuO catalysts.

2.2. Catalytic Performance Testing

Protection time is an important parameter for the evaluation of catalyst performance [9]. Figure 11 presents the protection times of the six catalysts against DMMP, as shown in Table 3. The protection times of the catalysts were ranked in the following order: 50%Cu/Ce (322 min) > 20%Cu/Ce (266 min) > 10%Cu/Ce (252 min) > 80%Cu/Ce (140 min) > CeO_2 (140 min) > CuO (56 min). The protection time of the CuO/CeO_2 catalyst was significantly improved after loading with CuO. The protection time first increased and then decreased with an increasing Cu/Ce ratio, and 50%Cu/Ce exhibited the longest protection time. The variation trend of protection time is the same as that of oxygen vacancy concentration in Raman, indicating that the importance of oxygen vacancies in the catalytic DMMP reaction. A comparison of protection time on various reported catalysts is summarized in Table 5.

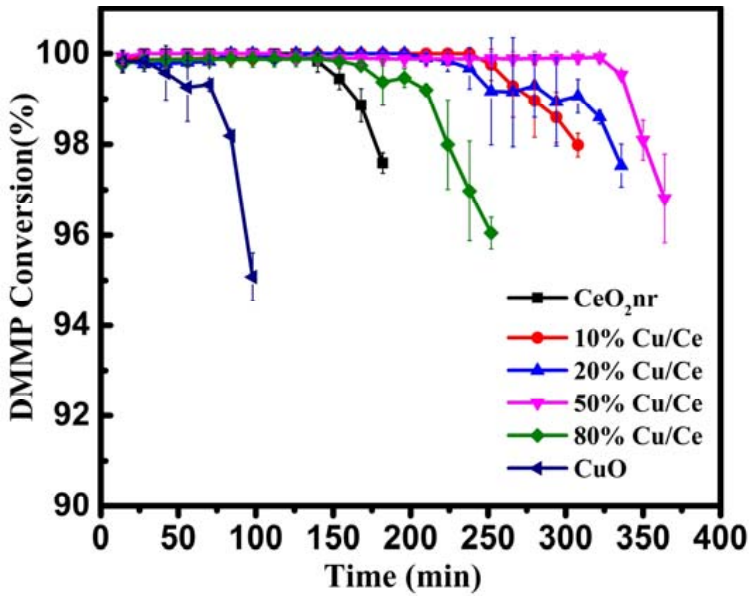

Figure 11. Effects of different Cu/Ce ratios of the CeO_2-supported CuO catalysts on protection time. Reaction temperature, 400 °C; inlet DMMP concentration, 8.46 g/m^3; catalyst weight, 0.46 g CuO/CeO_2 catalysts; size, 20–40 mesh; and GHSV, 20,000 h^{-1}.

Table 5. A comparison of protection time on various catalysts.

Catalyst	Reaction Condition	Protection Time	Reference
0.5%Pt-Al_2O_3	396 °C; DMMP concentration, 3.5 g/m^3; flow rate 8.85 L/min	12 h	Graven et al. [56]
Cu_2-HA	400 °C; DMMP concentration, 3.58 g/m^3; flow rate, 100 mL/min	7.5 h	Lee et al. [57]
1.2%Pt-Al_2O_3	400 °C; DMMP concentration, 3.58 g/m^3; flow rate, 100 mL/min	17 h	
10% V/Al_2O_3	400 °C; DMMP concentration 1300 ppm; flow rate, 50 mL/min	12.5 h	Cao et al. [9]
1% Pt/Al_2O_3		8.5 h	
10% Cu/Al_2O_3		7.5 h	
Al_2O_3		4.0 h	
10% Fe/Al_2O_3		3.5 h	
10% Ni/Al_2O_3		1.5 h	
10% V/SiO_2		25 h	
CeO_2	400 °C; DMMP concentration, 8.46 g/m^3; flow rate, 100 mL/min	2.33 h	This work
10%Cu/Ce		4.2 h	
20%Cu/Ce		4.43 h	
50%Cu/Ce		5.36 h	
80%Cu/Ce		2.33 h	
CuO		0.93 h	

2.3. Reaction Mechanism for the Thermocatalytic Decomposition of DMMP

50%Cu/Ce catalyst with the longest protection time, CeO_2, and CuO were selected to investigate the DMMP thermocatalytic decomposition mechanism. After the protection-time test, XPS analyses were performed on the deactivated catalyst; the results are shown in Figure 12. A P2p peak was obvious on the spent catalysts, indicating that the deactivated catalyst surface was covered with P species. The O1s spectrum of the deactivated catalyst was fitted to four peaks, namely surface lattice oxygen (Oα), P–O, adsorbed oxygen (O_{Ads}), and adsorbed water/hydroxyl oxygen [19]. The appearance of the P–O peak indicates the formation of P–O byproducts on the catalyst surface. Oα contents before and after the catalytic decomposition of DMMP were calculated (Table 6). It is obvious that the proportion of Oα in the deactivated catalyst was significantly lower that of the fresh catalyst, which indicates that lattice oxygen participates in the reaction and may play an important role in the catalytic oxidative decomposition of DMMP. Figure 12c shows the Cu2p spectra of CuO before and after the reaction. The $Cu2p_{3/2}$ peak changed from 534 to 535.5 eV, with a broad satellite peak at 935–945 eV. The Cu2p satellite peak of CuO in the deactivated catalyst was similar to that of $Cu2p_{3/2}$ when comparing the Cu2p of copper carbonate and copper phosphate, and the peak position was consistent with that of $Cu2p_{3/2}$. Therefore, copper phosphate and copper carbonate products were speculated to exist on the surface of the deactivated catalyst.

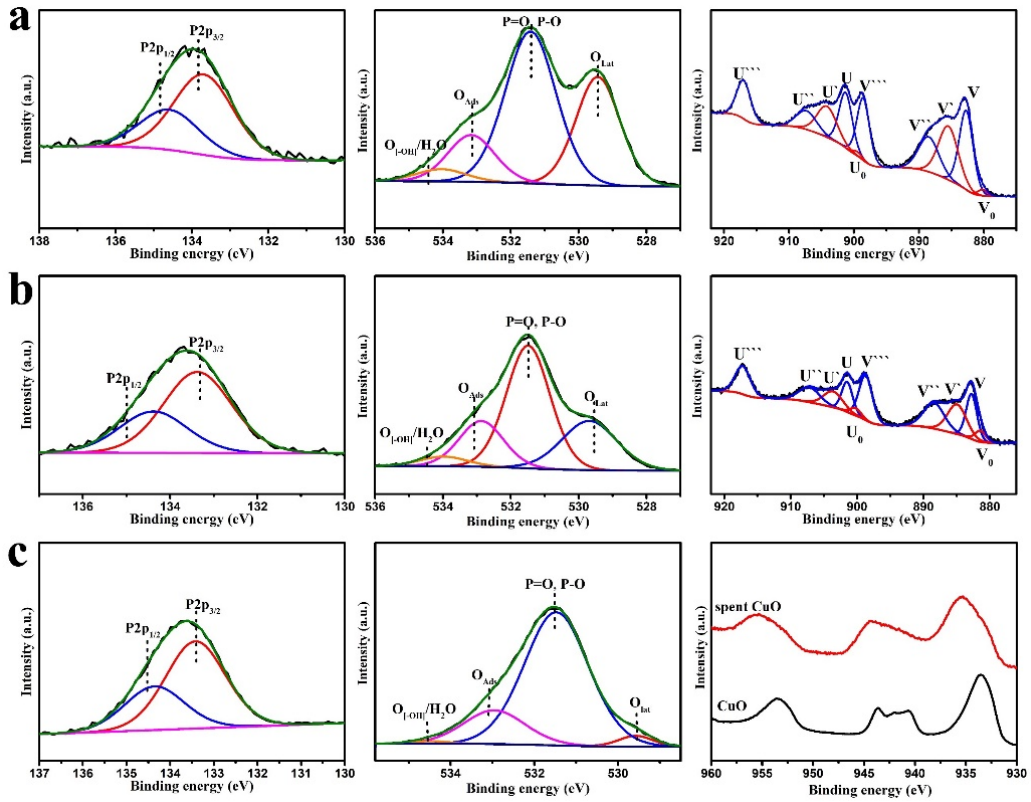

Figure 12. XPS spectra of the catalysts after the protection test: (**a**) CeO_2, (**b**) 50%Cu/Ce, and (**c**) CuO.

Table 6. Oα contents before and after the catalytic decomposition of DMMP.

Catalyst	Before Decomposition Reaction Oα	After Decomposition Reaction Oα
CeO_2	73.02%	37.94%
50%CuCe	75.88%	25.74%
CuO	66.36%	5.57%

The phosphorus-containing byproducts on the surface of the deactivated catalysts were qualitatively analyzed using ion chromatography, which showed the presence of PO_4^{3-} and methyl phosphonate species, as shown in Table 7. DMMP decomposition amounts and the corresponding P element amounts are presented in Table 7. Mass spectrometry was used to qualitatively analyze the tail gas produced by the catalytic decomposition of DMMP on CeO_2, 50%Cu/Ce, and CuO to determine its composition. Figure 13 shows the mass spectra of the tail gas generated by CeO_2, 50%Cu/Ce, and CuO, demonstrating that methanol, CO_2, H_2O, and H_2 were detected in the reaction tail gas. Additionally, except for the fragment mass-to-charge ratio of methanol and CO_2 (28), the mass-to-charge ratio of CO was 28. Therefore, gas chromatography was used to determine the presence of CO in the generated exhaust gas. CO was detected in the reaction tail gas of CeO_2 and CuO; however, no CO was detected for 50%Cu/Ce, indicating that the oxidative activity of the 50%Cu/Ce catalyst was higher than that of CeO_2 and CuO.

Table 7. Content of PO_4^{3-}, methyl phosphonate species, DMMP decomposition, and P element on various catalysts after the catalytic decomposition of DMMP.

Sample	PO_4^{3-} (mg/g)	Methyl Phosphonate Species (mg/g)	DMMP (mg/g)	P (mg/g)
CeO_2	3.1048	1.9941	257.5	64.13
50%Cu/Ce	0.2277	0.4502	592.17	147.48
CuO	1.6279	0.4276	102.7	25.57

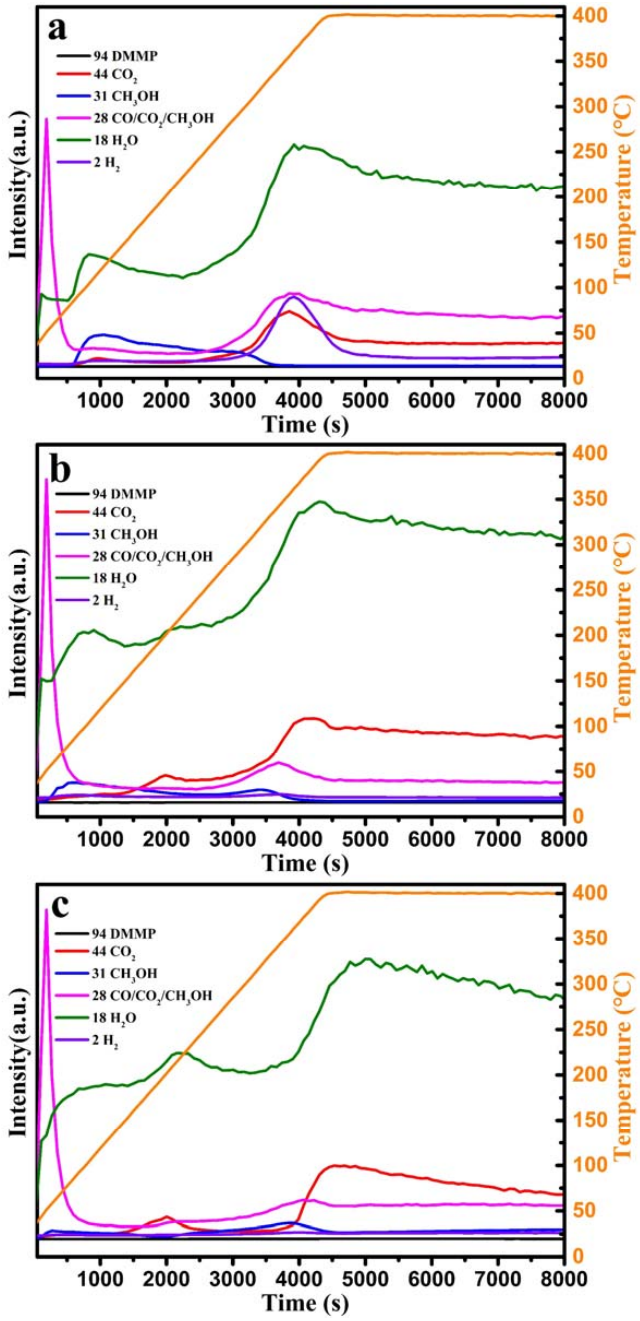

Figure 13. Mass spectrometry analysis of the tail gas generated from DMMP thermocatalytic decomposition on (**a**) CeO_2, (**b**) 50%Cu/Ce, and (**c**) CuO.

The in situ DRIFTS of DMMP on CeO_2, 50%Cu/Ce, and CuO at varying temperatures were determined to ascertain the species change of DMMP on the surface of the three catalysts. As shown in Figure 1, the molecular structure of DMMP contains P–CH_3, O–CH_3,

P=O, P–O, P–C, C–O, and C–H bonds. The vibration peaks of chemical bonds in DMMP are mainly distributed in two regions. C–H bond-stretching vibrations of P–CH_3 and O–CH_3 are located in the high-frequency region from approximately 2800 cm^{-1} to 3200 cm^{-1}, whereas stretching vibrations of P=O, C–O, and P–O, as well as deformation vibrations and rocking vibrations of PCH_3 and OCH_3 are located in the low-frequency region from 800 cm^{-1} to 1500 cm^{-1}. The corresponding functional groups of the DMMP molecules were consistent with those reported in the literature [58,59], as shown in Table 8. The corresponding functional groups of surface species on CeO_2, 50%Cu/Ce, and CuO are shown in Table 9. The characteristic peak located at 3500–3800 cm^{-1} was attributed to the stretching vibration of the surface hydroxyl groups [60,61]. As the temperature increased, hydroxyl vibration peaks of the negative-going OH bands were observed. The depletion of the surface hydroxyl groups may have originated from the formation of H bonds between the DMMP molecules and surface hydroxyl groups of CeO_2, CuO, and Cu/Ce or from the surface hydroxyl groups participating in the DMMP decomposition reaction [59,62] (Figures 14–16). Figure 14a shows the in situ DRIFTS of CeO_2 in the high-frequency region.

Table 8. IR frequencies and assignments of DMMP.

Vibrational Mode	IR Frequencies (cm^{-1})		
	DMMP [40]	DMMP Gas Phase [41]	DMMP Liquid Phase This Study
ν_a(P–CH_3)	2992	3014	2996
ν_a(O–CH_3)	2957	2962	2958
ν_s(P–CH_3)	2926	2924	2927
ν_s(O–CH_3)	2852	2860	2854
δ_a(O–CH_3)	1465	1467	1465
δ_s(O–CH_3)	1450	/	/
δ_s(P–CH_3)	1317	1314	1315
ν(P=O)	1242	1276	1257
ρ‖(O–CH_3)	1186	1188 (1190)	1187
ν_a(C–O)	1058	1070	1061
ν_s(C–O)	1034	1049	1034
ρ‖(P–CH_3)	916	914	914
ν(P–O)	822	816	821
ν(P–O)	789	/	/
ν(P–C)	714	/	/

Table 9. IR frequencies and assignments of the surface species.

Vibrational Mode	IR Frequencies (cm^{-1})		
	CeO_2	50%Cu/Ce	CuO
ν(OH)	3707	3706	3730
ν(OH)	3685	3685	/
ν(OH)	3663	3642	3606
ν_a(P–CH_3)	2944	2993	2985
ν_a(O–CH_3)	2913	2949	2954
ν_s(P–CH_3)	2889	2925	2928
ν_s(O–CH_3)	2834	/	2860
ν_a(C–H)	2931	/	/
ν_s(C–H)	2846	2849	/
ν(Ce–O–CH_3)	2803	2805	/
ν(Cu–O–CH_3)	/	/	2820
2δ(C–H)	2722	/	/
ν(OCO)	1572–1564	/	/
ν(OCO)	1537	/	/
δ(CH)	1368	/	/
ν(CO_3)	1357	/	/
δ_s(P–CH_3)	/	1307	1312
ν(P–O)	/	1152/1150	/
ν(OPO)	1097/1087/1075	1094	1055
ν(C–O)	1035	1036/1010	1032
ρ‖(P–CH_3)	/	903–893	918`

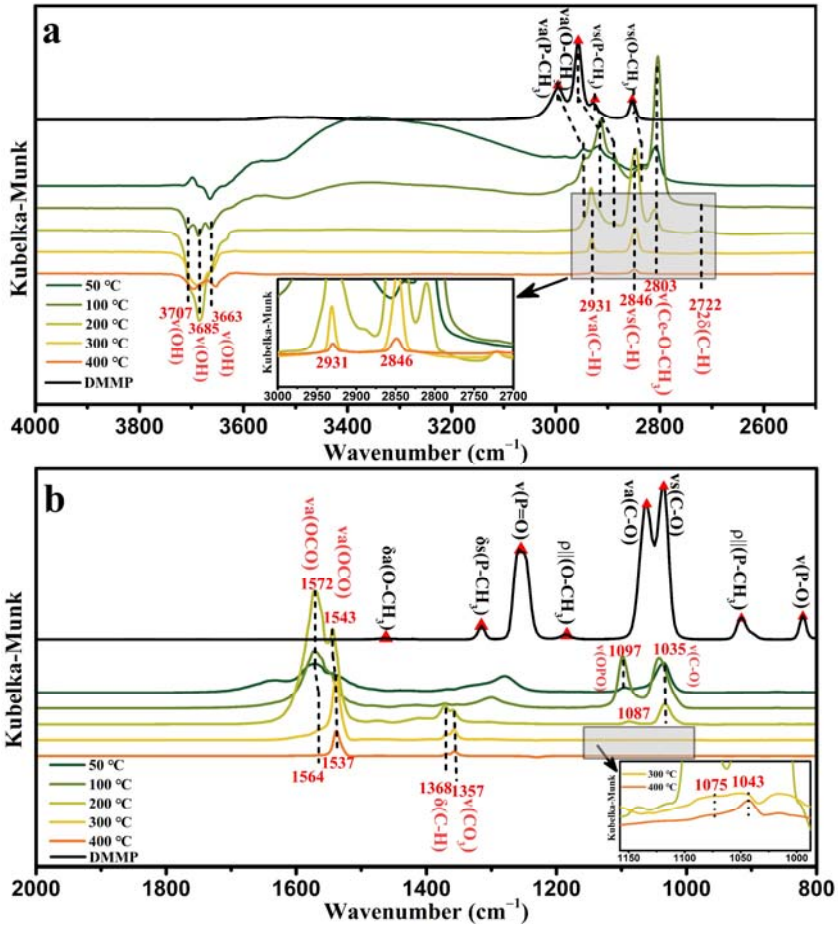

Figure 14. In situ DRIFTS spectra of CeO_2 at varying temperatures in (**a**) the high-frequency region and (**b**) in the mid–low frequency region, the inset is a magnified image of the tagged area.

The characteristic infrared peaks of ν_a(P–CH_3), ν_a(O–CH_3), ν_s(P–CH_3), and ν_s(O–CH_3) in the DMMP molecules gradually weakened with increasing temperature and disappeared at 400 °C. New characteristic peaks simultaneously appeared at 2931 cm^{-1} and 2846 cm^{-1}, and the peak intensity weakened with increasing temperature. Therefore, we speculated that these two peaks correspond to the ν(C–H) vibrational modes of the intermediates generated during DMMP decomposition. Morris et al. reported that cleavage of P–OCH_3 led to the formation of methoxy groups, which combined with Ti ions to form surface methoxy groups. The vibrational peak of the surface methoxy shifts to a lower frequency than that of DMMP [63]. A similar phenomenon was observed in the in situ DRIFTS of CeO_2. Therefore, the peak at 2803 cm^{-1} was attributed to ν(Ce–O–CH_3). Figure 14a shows a partially enlarged view of the 2600–2900 cm^{-1} band in the high-frequency region, which clearly demonstrates that the peak disappeared when the temperature reached 400 °C. This indicates that the methoxy group in Ce–O–CH_3 is an unstable intermediate product that can be completely decomposed by the CeO_2 catalyst at 400 °C. The vibrational peak at 2722 cm^{-1} shown in Figure 14a was assigned to the 2δ(C–H) vibrational mode of the formate product [61]. The characteristic infrared peaks of DMMP molecules in the mid–low frequency range of CeO_2 in situ DRIFTS (Figure 14b), δ_a(O–CH_3), δ_a(P–CH_3), ν(P=O), ρ‖(O–CH_3), ν_a(C–O), ν_s(C–O), ρ‖(P–CH_3), and ν(P–O), disappeared at 400 °C. The vibrational peaks at 1572–1564 cm^{-1} and 1537 cm^{-1} belong to the vibrational mode of bidentate (bdt) formate ν_a(OCO), and the δ(CH) vibrational mode of the formate appeared at 1368 cm^{-1} [61]. Additionally, the vibrational mode ν(CO_3) of the carbonate appeared at 1357 cm^{-1} [60].

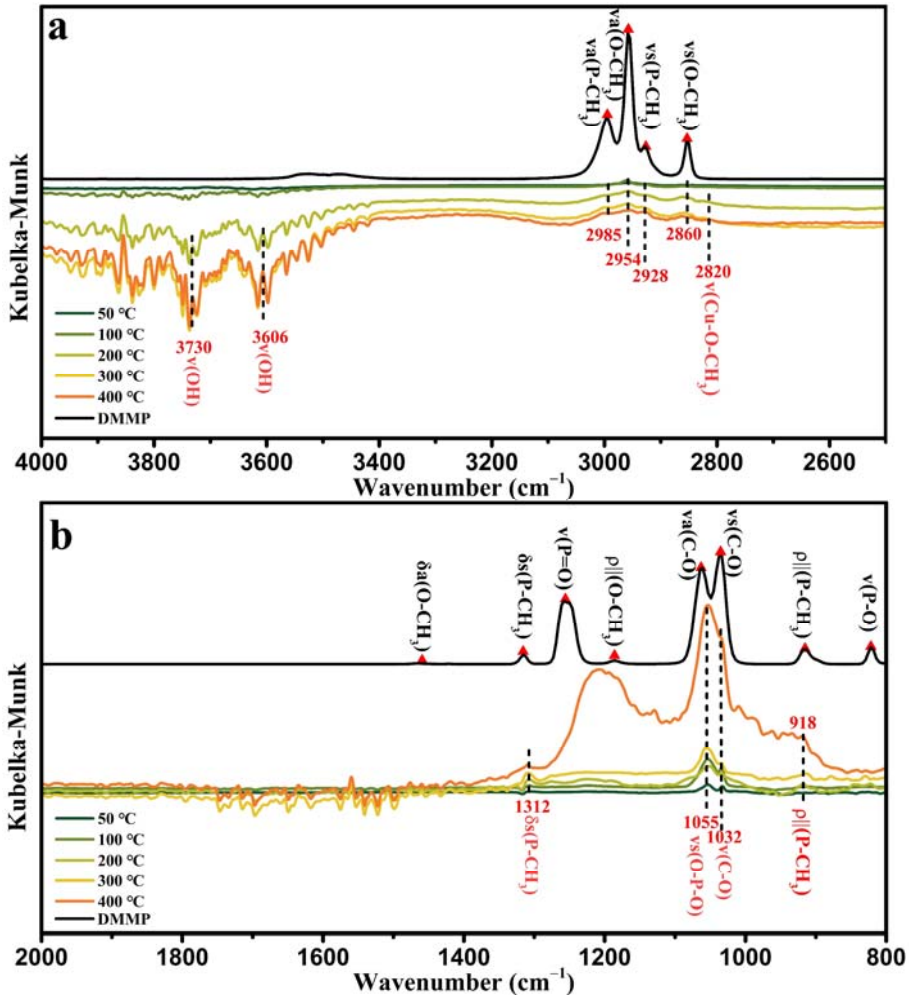

Figure 15. In situ DRIFTS spectra of CuO at varying temperatures in (**a**) the high-frequency region and (**b**) in the mid–low frequency region.

Figure 15 shows the in situ DRIFTS spectra of CuO at varying temperatures. CuO exhibited a multimodal overlap at 3100–2800 cm^{-1} in the high-frequency region of the in situ DRIFTS. Moreover, the in situ DRIFTS spectral peak signal of CuO in the high-frequency region was relatively weak, and it was impossible to directly distinguish the peak attribution in this region. The ν(C–H) characteristic peak of the intermediate product appeared in this region with reference to the in situ infrared spectrum of CeO_2 (Figure 15a). Therefore, we speculated that the CuO peaks in this region might be the ν(C–H) characteristic peaks of the undecomposed DMMP itself and the ν(C–H) characteristic peaks of the partially decomposed DMMP products. This is similar to the in situ DRIFTS spectrum of CeO_2; a ν(Cu–O–CH_3) vibrational peak was also generated on the CuO surface at 2820 cm^{-1}. The in situ DRIFTS (Figure 15b) in the mid–low frequency region clearly shows that the ν(P=O) vibration mode in DMMP disappeared, and a new bridging P species ν_s(O–P–O) appeared at 1055 cm^{-1}, implying an interaction between the phosphoryl oxide and catalyst surface [21,64]. The disappearance of the ν(P–O) vibration mode in DMMP indicated that the methoxy group was separated from the DMMP molecules, and the disappearance of the δ_a(O–CH_3), ρ‖(O–CH_3), ν_a(C–O), and ν_s(C–O) vibration modes in DMMP indicated that the methoxy group completely decomposed. Although the characteristic peaks of ρ‖(P–CH_3) and δ_s(P–CH_3) in DMMP were still visible, these characteristic peaks were speculated to be characteristic peaks of methyl-containing products. At 400 °C, the peak intensities of the two bands at 1290–1150 and 1100–1000 cm^{-1} significantly increased,

indicating that a large number of phosphorus and carbon oxygen products were produced on the surface of CuO at 400 °C [21,65].

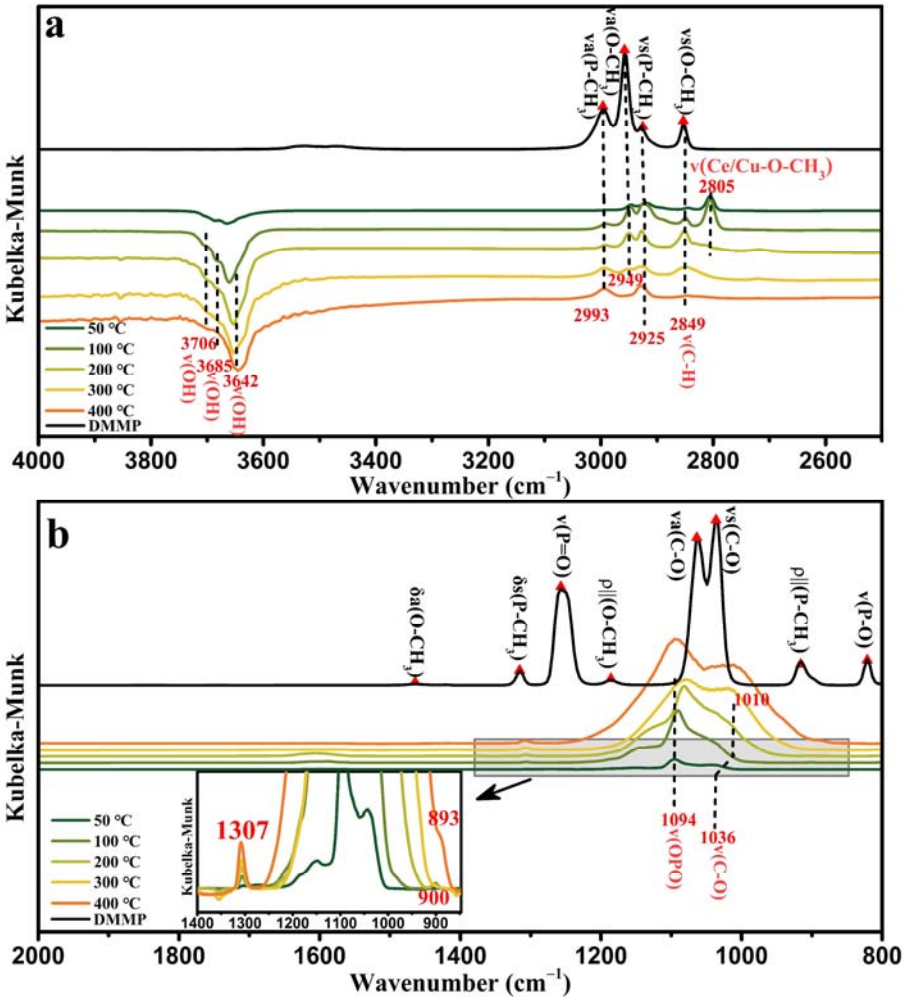

Figure 16. In situ DRIFTS spectra of 50%Cu/Ce at varying temperatures in (**a**) the high-frequency region and (**b**) in the mid–low frequency region, the inset is a magnified image of the tagged area.

Figure 16 shows the in situ DRIFTS spectra of 50%Cu/Ce at varying temperatures. In the in situ DRIFTS (Figure 16a) in the high-frequency region of 50%Cu/Ce, the stretching vibration mode ν_a(P–CH_3) of DMMP molecules shifted from 2996 to 2993 cm^{-1}; ν_s(P–CH_3) shifted from 2927 to 2925 cm^{-1}, and the peak did not decay with increasing temperature. Therefore, we speculated that the vibration peaks of ν(P–CH_3) at 2993 cm^{-1} and 2925 cm^{-1} were the DMMP decomposition products. The stretching vibration mode ν_a(O–CH_3) in DMMP shifted from 2958 to 2949 cm^{-1}, and the stretching vibration of ν_a(O–CH_3) weakened with increasing temperature, disappearing at 400 °C. The vibrational mode of ν_s(O–CH_3) in DMMP was similar to that of CeO_2; therefore, we speculated that the peak at 2849 cm^{-1} is the ν(C–H) vibrational mode of the intermediate product generated during the decomposition of DMMP. Similar to CeO_2 and CuO, the ν(Ce/Cu–O–CH_3) vibrational mode of the unstable intermediate appeared near 2805 cm^{-1} in the 50%Cu/Ce in situ DRIFTS and disappeared at 400 °C. The spectral characteristic peaks in the low-frequency region of the in situ DRIFTS (Figure 16b) of 50%Cu/Ce at 400 °C were similar to those of CuO, i.e., the methoxy group in DMMP completely decomposed. A methyl-containing product peak was present at 1307 cm^{-1}. Large quantities of phosphorus and carbon oxygen products were produced in the 1250–900 cm^{-1} band, and the magnified image of the 1350–850 cm^{-1} band shows that the 1307 cm^{-1} and 900–893 cm^{-1} bands are characteristic peaks of methyl-containing products.

The reaction pathways for the catalytic decomposition of DMMP on CeO_2, CuO, and CuO/CeO_2 were speculated using the combined ion chromatography, mass spectrometry, and in situ DRIFTS data (Scheme 1). Scheme 1(I) shows the presumed reaction pathway for the decomposition of DMMP on the surface of CeO_2. First, the electron-rich O in DMMP combines with Ce or surface hydroxyl groups on the surface of CeO_2. The surface hydroxyl groups nucleophilically attack P, breaking the P–OCH_3 bond, and combine the methoxy group with H to generate gaseous methanol. Simultaneously, methyl phosphates with bridged O–P–O structures formed on the surface [4,21,59] The surface lattice O in CeO_2 nucleophilically attacks the methyl group in methyl phosphate, forming a PO_x species on the CeO_2 surface, and the methyl group is further dehydrogenated to CO, H_2, CO_2, and H_2O (Scheme 1a). According to Wu et al., methanol can induce a series of side reactions on the CeO_2 surface [61]. First, in Scheme 1(II) methanol reacts with the CeO_2 surface lattice O to form surface methoxy Ce–O–CH_3. The methoxy groups continue to react with the surface lattice O or hydroxyl groups, fully dehydrogenating to form CO, H_2, CO_2, and H_2O (Scheme 1b) and partially dehydrogenating to form formate (Scheme 1c) [66], which reacts with the surface lattice O and completely dehydrogenates to form carbonate (Scheme 1d) [67]. Based on the in situ DRIFTS data, we speculated that the carbonates may contain one or more species, including polydentate, bidentate, bridged, and monodentate carbonates, due to the broadband nature of their vibrational modes. The catalytic decomposition pathways of DMMP on CuO and CuO/CeO_2 are essentially the same as those on CeO_2 (Scheme 1(I)). The difference is that there is no formate in the decomposition products of the CuO and CuO/CeO_2 catalytic decomposition of DMMP (Scheme 1c), and no CO is generated in the decomposition products of the CuO/CeO_2 catalytic decomposition of DMMP. This indicates that the synergistic effect of the bimetals enhances the selectivity for the fully catalytic oxidation product of DMMP, CO_2.

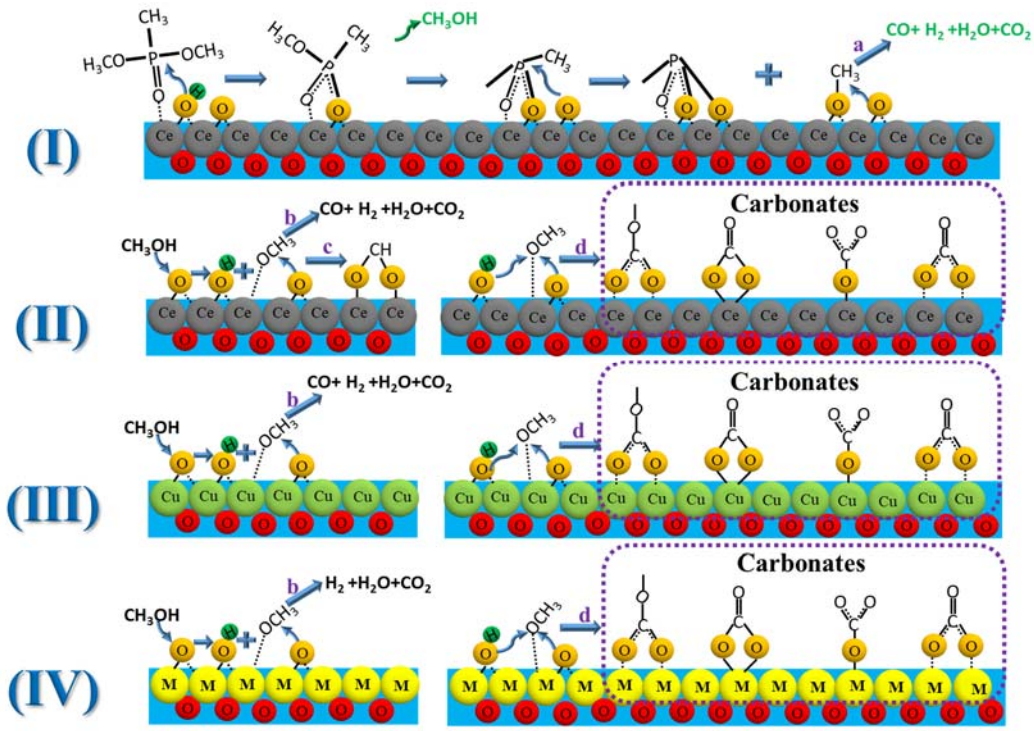

Scheme 1. Proposed reaction pathways for the decomposition of DMMP, (**I**) the main reaction pathway for the decomposition of DMMP on CeO_2, (**II**) the side reaction pathways for the decomposition of DMMP on CeO_2; (**III**) the side reaction pathways for the decomposition of DMMP on CuO; (**IV**) the side reactions pathways for the decomposition of DMMP on CuO/CeO_2 (M: Cu or Ce).

Various mechanisms have been proposed over ceria-based catalysts in the literature [68–70], which can be generally broken down into three main categories: the Eley-Rideal mechanism [71], the Langmuir-Hinshelwood mechanism [72], and the Mars-van-Krevelen mechanism [73,74]. In catalytic reactions at higher temperatures, the mechanism of CeO_2-based materials is mainly the Mars-van-Krevelen mechanism. The Mars-van-Krevelen mechanism consists of a redox cycle. First, reactant molecules interact with the lattice oxygen on the catalyst surface, and oxygen vacancies are formed on the catalyst surface. Then, the oxygen vacancies are refilled by gaseous oxygen or oxygen atoms from the bulk. Kinetic experimentation is needed in future studies to verify the thermal catalytic DMMP decomposition mechanism of as-prepared materials reported in the present study.

3. Materials and Methods

3.1. Synthesis of CeO_2 Catalyst

$Ce(NO_3)_3{\cdot}6H_2O$ (99.9%) and NaOH (99.9%) were obtained from Macklin, Shanghai, China. First, 2.6 g $Ce(NO_3)_3{\cdot}6H_2O$ was dissolved in deionized water (10 mL). Then, 21.6 g NaOH was dissolved in 45 mL of deionized water. The $Ce(NO_3)_3$ solution was added dropwise to the NaOH solution and continuously stirred at room temperature for 30 min. This mixture was hydrothermally treated in 100 mL Teflon-lined autoclaves for 24 h at 100 °C. After naturally cooling to room temperature, the products were centrifuged and washed several times with deionized water and ethanol. The precipitate was dried at 100 °C for 8 h and used for the synthesis of CuO/CeO_2 catalysts. Then, the precipitate was calcined at 400 °C for 4 h and used for characterization, catalytic performance testing, and reaction mechanism analysis.

3.2. CuO/CeO_2 Catalyst Preparation

A secondary alkaline hydrothermal approach was adopted to load CuO on CeO_2 nanorod supports to synthesize CuO/CeO_2 catalysts. Specifically, 3 g of the precipitates was fully dispersed in 10 mL of deionized water, including the calculated amount of $Cu(NO_3)_2{\cdot}3H_2O$, and slurries were obtained with 30 min of continuous stirring. Then, 10.8 g of NaOH was dissolved in 45 mL of deionized water. The NaOH solution was dropped into the slurry and stirred for 30 min. The mixture slurries were hydrothermally treated in a 100 mL Teflon-lined autoclave for 24 h at 100 °C. After naturally cooling to room temperature, the products were centrifuged and washed several times with deionized water and ethanol, dried at 100 °C for 8 h, and calcined at 400 °C for 4 h in air. Four types of CuO/CeO_2 catalysts were prepared using 0.87, 1.74, 4.36, and 6.97 g of $Cu(NO_3)_2{\cdot}3H_2O$ and labeled as 10%Cu/Ce, 20%Cu/Ce, 50%Cu/Ce, and 80%Cu/Ce, respectively.

3.3. Synthesis of CuO Catalyst

CuO was prepared using a hydrothermal method. First, 8.7 g of $Cu(NO_3)_2{\cdot}3H_2O$ was fully dispersed in deionized water (10 mL). Then, 10.8 g of NaOH was dissolved in 45 mL of deionized water. The $Cu(NO_3)_2$ solution was added dropwise to the NaOH solution and continuously stirred at room temperature for 30 min. This mixture was hydrothermally treated in 100 mL Teflon-lined autoclaves for 24 h at 100 °C. After naturally cooling to room temperature, the products were centrifuged and washed several times with deionized water and ethanol. The precipitates were dried at 100 °C for 8 h and calcined at 400 °C for 4 h in air.

3.4. Characterization of CuO/CeO_2 Catalysts

XRD analyses were performed on a 9 kW SmartLab (Rigaku, Saitama, Japan) with Cu Kα radiation (λ = 1.5418 Å). The Cu and Ce contents were analyzed using inductively coupled plasma optical emission spectrometry (ICP-OES; Agilent 725 ES, Santa Clara, CA, USA). N_2 adsorption–desorption measurements were performed on a Nova 4200e Quantachrome surface area analyzer (Quantachrome Instruments, Boynton Beach, FL, USA) at 77 K and calculated using the Brunauer–Emmett–Teller (BET) model. TEM images

and energy-dispersive X-ray spectroscopy (EDX) images of the samples were obtained using a TECNAI F20 electron microscope. H_2-TPR was performed using an AutoChem II 2920 instrument (Micromeritics, Norcross, GA, USA). The samples (60 mg) were heated to 300 °C at 50 mL/min of He for 3 h and cooled to 50 °C. Temperature-programmed reduction was performed by heating the sample at 10 °C/min from 50 to 900 °C in an H_2/Ar mixture (10% H_2, 90% Ar, 50 mL/min). O_2-TPD analyses were performed on an AutoChem II 2920 (Micromeritics, Norcross, GA, USA) as follows. The sample (60 mg) was first treated with He (50 mL/min) at 300 °C for 3 h to remove adsorbed impurities. After cooling to 50 °C, the sample was exposed to O_2/Ar (10% O_2, 90% Ar, 30 mL/min) for 1 h. Then, the sample was purged with He (30 mL/min) for 1 h. Finally, the sample was heated to 800 °C at 10 °C/min in He (30 mL/min). XPS measurements were conducted using a Thermo Fisher ESCALAB 250Xi (Waltham, MA, USA) system with Al-Kα radiation. The binding energy was calibrated using the C 1s peak (284.8 eV) as the internal standard. The XPS data were analyzed using Avantage software v5.976 (Thermo Fisher). All peaks of the corrected spectra were fitted with a Gaussian–Lorentzian shape function to fit the data. Raman spectroscopy was performed on a HORIBA LabRAM HR Evolution (Longjumeau, France) with 532 nm laser excitation. In situ DRIFTS spectra were acquired during the reaction process using a Nicolet iS50 instrument (Thermo Fisher Scientific, Waltham, MA, USA) to monitor the DMMP thermal catalytic decomposition reaction. During the reaction, 64 scans were recorded at an 8 cm^{-1} resolution (to minimize collection time) to form the spectra shown.

3.5. Thermal Catalytic Decomposition Performance Tests

The performances of the catalysts were evaluated using a custom-built catalytic evaluation system (Figure 17). Compressed air at 100 mL/min was used as the carrier gas. The compressed air flowed through a bubbler filled with DMMP at 30 °C to create a DMMP vapor stream. To avoid DMMP vapor condensation, the temperature of the gas line was maintained at 100 °C. Under these conditions, the inlet DMMP concentration was 8.46 g/m^3. A gas chromatograph (Agilent 6890N, chromatographic column DB-1701, Santa Clara, CA, USA) equipped with a flame ionization detector was used for online analysis. A blank DMMP decomposition experiment was conducted in an empty reactor to verify the thermal stability of DMMP at 400 °C. Then, 0.46 g of CuO/CeO_2 catalysts (20–40 mesh) was loaded in a 4 mm reaction tube with a catalytic temperature of 400 °C and a gas hourly space velocity (GHSV) of 20,000 h^{-1}. The catalytic decomposition performance was expressed in terms of the protection time (Protection time is defined as the duration of DMMP conversion at 100%). The DMMP conversion rate is defined by Equation (1).

$$\text{DMMP conversion rate} = \left(1 - \frac{C_{out}}{C_{in}}\right) \times 100\% \quad (1)$$

where C_{out} is the content of DMMP in the reaction tail gas, and C_{in} is the initial content of DMMP created by the bubbler.

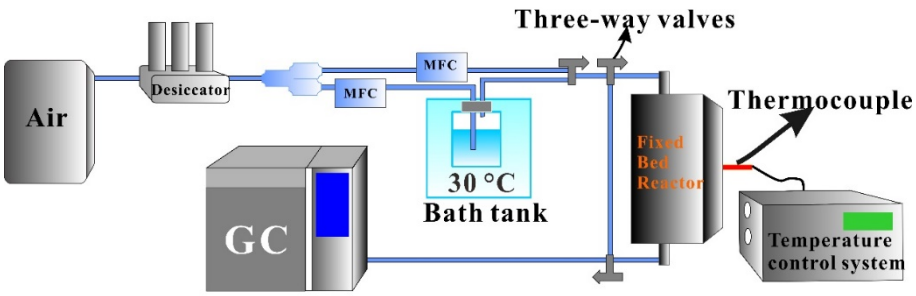

Figure 17. Schematic diagram of the catalytic evaluation system. MFC denotes mass flow meter, and the reaction tube size is 4 mm.

3.6. Characterization of Products in the Thermal Catalytic Decomposition Reaction

Thermal catalytic decomposition microreactions were performed in a CATLAB microreactor (Hiden Analytical, Warrington, UK). First 0.05 g CuO/CeO_2 was loaded in the reaction tube and dried for 2 h at 300 °C under He (100 mL/min). After the sample naturally cooled to room temperature, it was heated to 400 °C at 10 °C/min. A given concentration of DMMP vapor was introduced to the reaction tube using an 80% Ar and 20% O_2 mixture bubbled in a flask containing DMMP at 10 °C with a constant flux of 50 mL/min. The reaction tail gas was monitored using an HPR-20 mass spectrometer (Hiden Analytical, Warrington, UK). Ion chromatography was performed on an ICS-5000 instrument (Thermo Scientific, Waltham, MA, USA). The spent catalyst was dissolved in aqua regia and hydrofluoric acid, with a 15 mM KOH buffer used as eluent.

4. Conclusions

CeO_2 nanorods were used as catalyst supports to prepare CuO/CeO_2 catalysts with varying loading ratios using a secondary hydrothermal method. The addition of NaOH during the secondary hydrothermal process partially dissolved CeO_2. During the recrystallization process, Cu was doped into the CeO_2 lattice, resulting in more defects in the CeO_2 lattice and the formation of a Cu–V–Ce structure, which facilitated oxygen transfer. This preparation method provides a new and feasible method for lattice-doped bimetallic catalysts. Furthermore, the performance of CeO_2, CuO/CeO_2, and CuO in the thermal catalytic decomposition of DMMP was investigated. The load of CuO considerably improved the protection time as compared to the CeO_2 and CuO catalysts. Among the Cu/Ce catalysts with varying ratios, the protection time first increased and then decreased with an increasing loading ratio, and the 50%Cu/Ce catalyst had the longest protection time. A strong interaction was generated between CeO_2 and CuO through electron transfer, and the bimetallic synergy between Cu and Ce enhanced the catalytic decomposition performance of the CeO_2. The catalytic reaction pathways of CeO_2, CuO, and CuO/CeO_2 were similar, and the gas-phase products were CH_3OH, CO_2, H_2O, and H_2. However, CO was still present in the gas-phase products of CeO_2 and CuO, whereas the gas phase of CuO/CeO_2 was CO_2, indicating that the CuO/CeO_2 bimetallic catalyst had higher selectivity for CO_2. Carbonate and formate byproducts were formed on the CeO_2 catalyst surface, whereas only carbonates were formed on the surfaces of the CuO and CuO/CeO_2 catalysts. The accumulation of P–O and C–O products on the surface of the three catalysts resulted in their eventual deactivation. This study preliminarily revealed the mechanism of the CuO/CeO_2 catalyst for catalysis of the decomposition of DMMP, which can inform the design of catalysts for the efficient degradation of chemical poisons in the future.

Author Contributions: W.K. and S.Z. designed the experiments, made the main contribution to the experimental works, and managed the experimental and writing process as co-first authors; X.W. and Q.H. assisted in accomplishing a part of the experimental works and characterizations; S.Z., P.Y. and Y.D. provided the concept of this research, participated in the guidance of this work, and provided advice on the synthesis of CeO_2 supports and catalyst characterization as the corresponding authors. Y.Y. participated in the guidance of this work and provided advice on the synthesis of CeO_2 supports and catalyst characterization as the corresponding authors. All authors have read and agreed to the published version of the manuscript.

Funding: This work was financially supported by the National Natural Science Foundation of China (No. 21701186) and the Fundamental Research Funds from State Key Laboratory of NBC Protection for Civilian (SKLNBC 2019-04), China.

Conflicts of Interest: The authors declare no conflict of interest.

References

1. Jang, Y.J.; Kim, K.; Tsay, O.G.; Atwood, D.A.; Churchill, D.G. Update 1 of: Destruction and Detection of Chemical Warfare Agents. *Chem. Rev.* **2015**, *115*, PR1–PR76. [CrossRef] [PubMed]
2. Monji, M.; Ciora, R.; Liu, P.K.T.; Parsley, D.; Egolfopoulos, F.N.; Tsotsis, T.T. Thermocatalytic decomposition of dimethyl methylphosphonate (DMMP) in a multi-tubular, flow-through catalytic membrane reactor. *J. Membr. Sci.* **2015**, *482*, 42–48. [CrossRef]
3. Nawala, J.; Jozwik, P.; Popiel, S. Thermal and catalytic methods used for destruction of chemical warfare agents. *Int. J. Environ. Sci. Technol.* **2019**, *16*, 3899–3912. [CrossRef]
4. Mitchell, M.B.; Sheinker, V.N.; Mintz, E.A. Adsorption and Decomposition of Dimethyl Methylphosphonate on Metal Oxides. *J. Phys. Chem. B* **1997**, *101*, 11192–11203. [CrossRef]
5. Mitchell, M.B.; Sheinker, V.N.; Cox, W.W.; Gatimu, E.N.; Tesfamichael, A.B. The Room Temperature Decomposition Mechanism of Dimethyl Methylphosphonate (DMMP) on Alumina-Supported Cerium Oxide—Participation of Nano-Sized Cerium Oxide Domains. *J. Phys. Chem. B* **2004**, *108*, 1634–1645. [CrossRef]
6. Bermudez, V.M. Quantum-Chemical Study of the Adsorption of DMMP and Sarin on γ-Al_2O_3. *J. Phys. Chem. C* **2007**, *111*, 3719–3728. [CrossRef]
7. Gordon, W.O.; Tissue, B.M.; Morris, J.R. Adsorption and decomposition of dimethyl methylphosphonate on Y_2O_3 nanoparticles. *J. Phys. Chem. C* **2007**, *111*, 3233–3240. [CrossRef]
8. Mukhopadhyay, S.; Schoenitz, M.; Dreizin, E.L. Vapor-phase decomposition of dimethyl methylphosphonate (DMMP), a sarin surrogate, in presence of metal oxides. *Def. Technol.* **2021**, *17*, 1095–1114. [CrossRef]
9. Cao, L.; Segal, S.R.; Suib, S.L.; Tang, X.; Satyapal, S. Thermocatalytic Oxidation of Dimethyl Methylphosphonate on Supported Metal Oxides. *J. Catal.* **2000**, *194*, 61–70. [CrossRef]
10. Gupta, R.C. (Ed.) *Handbook of Toxicology of Chemical Warfare Agents*; Academic Press Ltd.; Elsevier Science Ltd.: London, UK, 2009.
11. Woo, T.G.; Cha, B.J.; Kim, Y.D.; Seo, H.O. Positive Effects of Impregnation of Fe-oxide in Mesoporous Al-Oxides on the Decontamination of Dimethyl Methylphosphonate. *Catalysts* **2019**, *9*, 898. [CrossRef]
12. Zammataro, A.; Santonocito, R.; Pappalardo, A.; Trusso Sfrazzetto, G. Catalytic Degradation of Nerve Agents. *Catalysts* **2020**, *10*, 881. [CrossRef]
13. Liu, Y.; Howarth, A.J.; Vermeulen, N.A.; Moon, S.-Y.; Hupp, J.T.; Farha, O.K. Catalytic degradation of chemical warfare agents and their simulants by metal-organic frameworks. *Coord. Chem. Rev.* **2017**, *346*, 101–111. [CrossRef]
14. Picard, B.; Chataigner, I.; Maddaluno, J.; Legros, J. Introduction to chemical warfare agents, relevant simulants and modern neutralisation methods. *Org. Biomol. Chem* **2019**, *17*, 6528–6537. [CrossRef]
15. Sheinker, V.N.; Mitchell, M.B. Quantitative Study of the Decomposition of Dimethyl Methylphosphonate (DMMP) on Metal Oxides at Room Temperature and Above. *Chem. Mater.* **2002**, *14*, 1257–1268. [CrossRef]
16. Zhanpeisov, N.U.; Zhidomirov, G.M.; Yudanov, I.V.; Klabunde, K.J. Cluster Quantum Chemical Study of the Interaction of Dimethyl Methylphosphonate with Magnesium Oxide. *J. Phys. Chem.* **1994**, *98*, 10032–10035. [CrossRef]
17. Panayotov, D.A.; Morris, J.R. Thermal Decomposition of a Chemical Warfare Agent Simulant (DMMP) on TiO_2: Adsorbate Reactions with Lattice Oxygen as Studied by Infrared Spectroscopy. *J. Phys. Chem. C* **2009**, *113*, 15684–15691. [CrossRef]
18. Walenta, C.A.; Xu, F.; Tesvara, C.; O'Connor, C.R.; Sautet, P.; Friend, C.M. Facile Decomposition of Organophosphonates by Dual Lewis Sites on a Fe_3O_4(111) Film. *J. Phys. Chem. C* **2020**, *124*, 12432–12441. [CrossRef]
19. Trotochaud, L.; Head, A.R.; Buchner, C.; Yu, Y.; Karslioglu, O.; Tsyshevsky, R.; Holdren, S.; Eichhorn, B.; Kuklja, M.M.; Bluhm, H. Room temperature decomposition of dimethyl methylphosphonate on cuprous oxide yields atomic phosphorus. *Surf. Sci.* **2019**, *680*, 75–87. [CrossRef]
20. Wang, L.; Denchy, M.; Blando, N.; Hansen, L.; Bilik, B.; Tang, X.; Hicks, Z.; Bowen, K.H. Thermal Decomposition of Dimethyl Methylphosphonate on Size-Selected Clusters: A Comparative Study between Copper Metal and Cupric Oxide Clusters. *J. Phys. Chem. C* **2021**, *125*, 11348–11358. [CrossRef]
21. Chen, D.A.; Ratliff, J.S.; Hu, X.; Gordon, W.O.; Senanayake, S.D.; Mullins, D.R. Dimethyl methylphosphonate decomposition on fully oxidized and partially reduced ceria thin films. *Surf. Sci.* **2010**, *604*, 574–587. [CrossRef]
22. Li, T.; Tsyshevsky, R.; Algrim, L.; McEntee, M.; Durke, E.M.; Eichhorn, B.; Karwacki, C.; Zachariah, M.R.; Kuklja, M.M.; Rodriguez, E.E. Understanding Dimethyl Methylphosphonate Adsorption and Decomposition on Mesoporous CeO_2. *ACS Appl. Mater. Interfaces* **2021**, *13*, 54597–54609. [CrossRef] [PubMed]
23. Montini, T.; Melchionna, M.; Monai, M.; Fornasiero, P. Fundamentals and Catalytic Applications of CeO_2-Based Materials. *Chem. Rev.* **2016**, *116*, 5987–6041. [CrossRef] [PubMed]
24. Wang, W.-W.; Du, P.-P.; Zou, S.-H.; He, H.-Y.; Wang, R.-X.; Jin, Z.; Shi, S.; Huang, Y.-Y.; Si, R.; Song, Q.-S.; et al. Highly Dispersed Copper Oxide Clusters as Active Species in Copper-Ceria Catalyst for Preferential Oxidation of Carbon Monoxide. *ACS Catal.* **2015**, *5*, 2088–2099. [CrossRef]
25. Reis, C.G.M.; Almeida, K.A.; Silva, T.F.; Assaf, J.M. CO preferential oxidation reaction aspects in a nanocrystalline CuO/CeO_2 catalyst. *Catal. Today* **2020**, *344*, 124–128. [CrossRef]
26. Delimaris, D.; Ioannides, T. VOC oxidation over CuO-CeO_2 catalysts prepared by a combustion method. *Appl. Catal. B Environ.* **2009**, *89*, 295–302. [CrossRef]

27. Djinović, P.; Batista, J.; Pintar, A. WGS reaction over nanostructured CuO–CeO_2 catalysts prepared by hard template method: Characterization, activity and deactivation. *Catal. Today* **2009**, *147*, S191–S197. [CrossRef]
28. Wang, Y.; Chen, Z.; Han, P.; Du, Y.; Gu, Z.; Xu, X.; Zheng, G. Single-Atomic Cu with Multiple Oxygen Vacancies on Ceria for Electrocatalytic CO_2 Reduction to CH_4. *ACS Catal.* **2018**, *8*, 7113–7119. [CrossRef]
29. Zhang, X.; Su, L.; Kong, Y.; Ma, D.; Ran, Y.; Peng, S.; Wang, L.; Wang, Y. CeO_2 nanoparticles modified by CuO nanoparticles for low-temperature CO oxidation with high catalytic activity. *J. Phys. Chem. Solids* **2020**, *147*, 109651. [CrossRef]
30. Xie, Y.; Wu, J.; Jing, G.; Zhang, H.; Zeng, S.; Tan, X.; Zou, X.; Wen, J.; Su, H.; Zhong, C.-J.; et al. Structural origin of high catalytic activity for preferential CO oxidation over CuO/CeO_2 nanocatalysts with different shapes. *Appl. Catal. B Environ.* **2018**, *239*, 665–676. [CrossRef]
31. Ren, Z.; Peng, F.; Li, J.; Liang, X.; Chen, B. Morphology-Dependent Properties of Cu/CeO_2 Catalysts for the Water-Gas Shift Reaction. *Catalysts* **2017**, *7*, 48. [CrossRef]
32. Kappis, K.; Papadopoulos, C.; Papavasiliou, J.; Vakros, J.; Georgiou, Y.; Deligiannakis, Y.; Avgouropoulos, G. Tuning the Catalytic Properties of Copper-Promoted Nanoceria via a Hydrothermal Method. *Catalysts* **2019**, *9*, 138. [CrossRef]
33. Papavasiliou, J.; Vakros, J.; Avgouropoulos, G. Impact of acid treatment of CuO-CeO_2 catalysts on the preferential oxidation of CO reaction. *Catal. Commun.* **2018**, *115*, 68–72. [CrossRef]
34. Papavasiliou, J.; Rawski, M.; Vakros, J.; Avgouropoulos, G. A Novel Post-Synthesis Modification of CuO-CeO_2 Catalysts: Effect on Their Activity for Selective CO Oxidation. *ChemCatChem* **2018**, *10*, 2096–2106. [CrossRef]
35. Guo, X.; Qiu, Z.; Mao, J.; Zhou, R. Doping effect of transition metals (Zr, Mn, Ti and Ni) on well-shaped CuO/CeO_2 (rods): Nano/micro structure and catalytic performance for selective oxidation of CO in excess H_2. *Phys. Chem. Chem. Phys. PCCP* **2018**, *20*, 25983–25994. [CrossRef]
36. López, J.M.; Gilbank, A.L.; García, T.; Solsona, B.; Agouram, S.; Torrente-Murciano, L. The prevalence of surface oxygen vacancies over the mobility of bulk oxygen in nanostructured ceria for the total toluene oxidation. *Appl. Catal. B Environ.* **2015**, *174–175*, 403–412. [CrossRef]
37. Tang, X.; Zhang, B.; Li, Y.; Xu, Y.; Xin, Q.; Shen, W. CuO/CeO_2 catalysts: Redox features and catalytic behaviors. *Appl. Catal. A Gen.* **2005**, *288*, 116–125. [CrossRef]
38. Wang, C.; Cheng, Q.; Wang, X.; Ma, K.; Bai, X.; Tan, S.; Tian, Y.; Ding, T.; Zheng, L.; Zhang, J.; et al. Enhanced catalytic performance for CO preferential oxidation over CuO catalysts supported on highly defective CeO_2 nanocrystals. *Appl. Surf. Sci.* **2017**, *422*, 932–943. [CrossRef]
39. Zou, Q.; Zhao, Y.; Jin, X.; Fang, J.; Li, D.; Li, K.; Lu, J.; Luo, Y. Ceria-nano supported copper oxide catalysts for CO preferential oxidation: Importance of oxygen species and metal-support interaction. *Appl. Surf. Sci.* **2019**, *494*, 1166–1176. [CrossRef]
40. Afzal, S.; Quan, X.; Lu, S. Catalytic performance and an insight into the mechanism of CeO_2 nanocrystals with different exposed facets in catalytic ozonation of *p*-nitrophenol. *Appl. Catal. B Environ.* **2019**, *248*, 526–537. [CrossRef]
41. Wang, Q.Y.; Yeung, K.L.; Banares, M.A. Operando Raman-online FTIR investigation of ceria, vanadia/ceria and gold/ceria catalysts for toluene elimination. *J. Catal.* **2018**, *364*, 80–88. [CrossRef]
42. Wang, F.; Büchel, R.; Savitsky, A.; Zalibera, M.; Widmann, D.; Pratsinis, S.E.; Lubitz, W.; Schüth, F. In Situ EPR Study of the Redox Properties of CuO–CeO_2 Catalysts for Preferential CO Oxidation (PROX). *ACS Catal.* **2016**, *6*, 3520–3530. [CrossRef]
43. Polster, C.S.; Nair, H.; Baertsch, C.D. Study of active sites and mechanism responsible for highly selective CO oxidation in H_2 rich atmospheres on a mixed Cu and Ce oxide catalyst. *J. Catal.* **2009**, *266*, 308–319. [CrossRef]
44. Sedmak, G.; Hočevar, S.; Levec, J. Kinetics of selective CO oxidation in excess of H_2 over the nanostructured $Cu_{0.1}Ce_{0.9}O_2$-catalyst. *J. Catal.* **2003**, *213*, 135–150. [CrossRef]
45. Liu, Z.; Wang, Q.; Wu, J.; Zhang, H.; Liu, Y.; Zhang, T.; Tian, H.; Zeng, S. Active Sites and Interfacial Reducibility of Cu_xO/CeO_2 Catalysts Induced by Reducing Media and O_2/H_2 Activation. *ACS Appl. Mater. Interfaces* **2021**, *13*, 35804–35817. [CrossRef]
46. Davó-Quiñonero, A.; Bailón-García, E.; López-Rodríguez, S.; Juan-Juan, J.; Lozano-Castelló, D.; García-Melchor, M.; Herrera, F.C.; Pellegrin, E.; Escudero, C.; Bueno-López, A. Insights into the Oxygen Vacancy Filling Mechanism in CuO/CeO_2 Catalysts: A Key Step Toward High Selectivity in Preferential CO Oxidation. *ACS Catal.* **2020**, *10*, 6532–6545. [CrossRef]
47. May, Y.A.; Wang, W.-W.; Yan, H.; Wei, S.; Jia, C.-J. Insights into facet-dependent reactivity of CuO–CeO_2 nanocubes and nanorods as catalysts for CO oxidation reaction. *Chin. J. Catal.* **2020**, *41*, 1017–1027. [CrossRef]
48. Davó-Quiñonero, A.; Such-Basáñez, I.; Juan-Juan, J.; Lozano-Castelló, D.; Stelmachowski, P.; Grzybek, G.; Kotarba, A.; Bueno-López, A. New insights into the role of active copper species in CuO/Cryptomelane catalysts for the CO-PROX reaction. *Appl. Catal. B Environ.* **2020**, *267*, 118372. [CrossRef]
49. Qi, L.; Yu, Q.; Dai, Y.; Tang, C.; Liu, L.; Zhang, H.; Gao, F.; Dong, L.; Chen, Y. Influence of cerium precursors on the structure and reducibility of mesoporous CuO-CeO_2 catalysts for CO oxidation. *Appl. Catal. B Environ.* **2012**, *119–120*, 308–320. [CrossRef]
50. Zhang, Y.D.; Liang, L.; Chen, Z.Y.; Wen, J.J.; Zhong, W.; Zou, S.B.; Fu, M.L.; Chen, L.M.; Ye, D.Q. Highly efficient Cu/CeO_2-hollow nanospheres catalyst for the reverse water-gas shift reaction: Investigation on the role of oxygen vacancies through in situ UV-Raman and DRIFTS. *Appl. Surf. Sci.* **2020**, *516*, 146035. [CrossRef]
51. Zhang, X.-m.; Tian, P.; Tu, W.; Zhang, Z.; Xu, J.; Han, Y.-F. Tuning the Dynamic Interfacial Structure of Copper–Ceria Catalysts by Indium Oxide during CO Oxidation. *ACS Catal.* **2018**, *8*, 5261–5275. [CrossRef]

52. He, C.; Yu, Y.; Yue, L.; Qiao, N.; Li, J.; Shen, Q.; Yu, W.; Chen, J.; Hao, Z. Low-temperature removal of toluene and propanal over highly active mesoporous $CuCeO_x$ catalysts synthesized via a simple self-precipitation protocol. *Appl. Catal. B Environ.* **2014**, *147*, 156–166. [CrossRef]
53. Torrente-Murciano, L.; Gilbank, A.; Puertolas, B.; Garcia, T.; Solsona, B.; Chadwick, D. Shape-dependency activity of nanostructured CeO_2 in the total oxidation of polycyclic aromatic hydrocarbons. *Appl. Catal. B Environ.* **2013**, *132–133*, 116–122. [CrossRef]
54. Deng, Y.Q.; Shi, X.B.; Wei, L.Q.; Liu, H.; Li, J.; Ou, X.M.; Dong, L.H.; Li, B. Effect of intergrowth and coexistence CuO-CeO_2 catalyst by grinding method application in the catalytic reduction of NO_x by CO. *J. Alloys Compd.* **2021**, *869*, 159231. [CrossRef]
55. Papadopoulos, C.; Kappis, K.; Papavasiliou, J.; Vakros, J.; Kuśmierz, M.; Gac, W.; Georgiou, Y.; Deligiannakis, Y.; Avgouropoulos, G. Copper-promoted ceria catalysts for CO oxidation reaction. *Catal. Today* **2020**, *355*, 647–653. [CrossRef]
56. Graven, W.M.; Weller, S.W.; Peters, D.L. Catalytic conversion of a organophosphate vapor over platinum-alumina. *Ind. Eng. Chem. Process Des. Dev.* **1966**, *5*, 183. [CrossRef]
57. Lee, K.Y.; Houalla, M.; Hercules, D.M.; Hall, W.K. Catalytic Oxidative Decomposition of Dimethyl Methylphosphonate over Cu-Substituted Hydroxyapatite. *J. Catal.* **1994**, *145*, 223–231. [CrossRef]
58. Lee, K.; Houalla, M.; Hercules, D.; Hall, W. Vibrational spectra and possible conformers of dimethylmethylphosphonate by normal mode analysis. *Spectrochim. Acta* **1989**, *45A*, 1015–1024.
59. Rusu, C.N.; Yates, J.T. Adsorption and Decomposition of Dimethyl Methylphosphonate on TiO_2. *J. Phys. Chem. B* **2000**, *104*, 12292–12298. [CrossRef]
60. Binet, C.; Daturi, M.; Lavalley, J.-C. IR study of polycrystalline ceria properties in oxidised and reduced states. *Catal. Today* **1999**, *50*, 207–225. [CrossRef]
61. Wu, Z.; Li, M.; Mullins, D.R.; Overbury, S.H. Probing the Surface Sites of CeO_2 Nanocrystals with Well-Defined Surface Planes via Methanol Adsorption and Desorption. *ACS Catal.* **2012**, *2*, 2224–2234. [CrossRef]
62. Kanan, S.M.; Lu, Z.; Tripp, C.P. A Comparative Study of the Adsorption of Chloro- and Non-Chloro-Containing Organophosphorus Compounds on WO_3. *J. Phys. Chem. B* **2002**, *106*, 9576–9580. [CrossRef]
63. Panayotov, D.A.; Morris, J.R. Uptake of a chemical warfare agent simulant (DMMP) on TiO_2: Reactive adsorption and active site poisoning. *Langmuir* **2009**, *25*, 3652–3658. [CrossRef] [PubMed]
64. Jeon, S.; Schweigert, I.V.; Pehrsson, P.E.; Balow, R.B. Kinetics of Dimethyl Methylphosphonate Adsorption and Decomposition on Zirconium Hydroxide Using Variable Temperature In Situ Attenuated Total Reflection Infrared Spectroscopy. *ACS Appl. Mater. Interfaces* **2020**, *12*, 14662–14671. [CrossRef] [PubMed]
65. Isahak, W.N.R.W.; Ramli, Z.A.C.; Ismail, M.W.; Ismail, K.; Yusop, R.M.; Hisham, M.W.M.; Yarmo, M.A. Adsorption–desorption of CO_2 on different type of copper oxides surfaces: Physical and chemical attractions studies. *J. CO2 Util.* **2013**, *2*, 8–15. [CrossRef]
66. Huttunen, P.K.; Labadini, D.; Hafiz, S.S.; Gokalp, S.; Wolff, E.P.; Martell, S.M.; Foster, M. DRIFTS investigation of methanol oxidation on CeO_2 nanoparticles. *Appl. Surface Sci.* **2021**, *554*, 149518. [CrossRef]
67. Albrecht, P.M.; Mullins, D.R. Adsorption and reaction of methanol over CeO(X)(100) thin films. *Langmuir* **2013**, *29*, 4559–4567. [CrossRef]
68. Ruiz Puigdollers, A.; Schlexer, P.; Tosoni, S.; Pacchioni, G. Increasing Oxide Reducibility: The Role of Metal/Oxide Interfaces in the Formation of Oxygen Vacancies. *ACS Catal.* **2017**, *7*, 6493–6513. [CrossRef]
69. Yang, C.; Miao, G.; Pi, Y.; Xia, Q.; Wu, J.; Li, Z.; Xiao, J. Abatement of various types of VOCs by adsorption/catalytic oxidation: A review. *Chem. Eng. J.* **2019**, *370*, 1128–1153. [CrossRef]
70. He, C.; Cheng, J.; Zhang, X.; Douthwaite, M.; Pattisson, S.; Hao, Z. Recent Advances in the Catalytic Oxidation of Volatile Organic Compounds: A Review Based on Pollutant Sorts and Sources. *Chem. Rev.* **2019**, *119*, 4471–4568. [CrossRef]
71. Bashir, S.M.; Idriss, H. The reaction of propylene to propylene-oxide on CeO_2: An FTIR spectroscopy and temperature programmed desorption study. *J. Chem. Phys.* **2020**, *152*, 044712. [CrossRef]
72. Hu, C.Q. Catalytic combustion kinetics of acetone and toluene over $Cu_{0.13}Ce_{0.87}O_y$ catalyst. *Chem. Eng. J.* **2011**, *168*, 1185–1192. [CrossRef]
73. Menon, U.; Galvita, V.V.; Constales, D.; Alexopoulos, K.; Yablonsky, G.; Marin, G.B. Microkinetics for toluene total oxidation over CuO–CeO_2/Al_2O_3. *Catal. Today* **2015**, *258*, 214–224. [CrossRef]
74. Mi, R.; Li, D.; Hu, Z.; Yang, R.T. Morphology Effects of CeO_2 Nanomaterials on the Catalytic Combustion of Toluene: A Combined Kinetics and Diffuse Reflectance Infrared Fourier Transform Spectroscopy Study. *ACS Catal.* **2021**, *11*, 7876–7889. [CrossRef]